Westfälische
Wilhelms-Universität
Münster

Calculation of Jet Cross Sections in Proton–Proton Collisions in Comparison with LHC Data

(Berechnung von Jet-Wirkungsquerschnitten in Proton-Proton-Kollisionen im Vergleich mit LHC-Daten)

Philipp Kähler, Master Thesis, 2015

wissen.leben
WWU Münster

Institut für Kernphysik
Westfälische Wilhelms-Universität

Ich erkläre, die vorliegende Arbeit selbständig verfasst, keine anderen als die angegebenen Quellen und Hilfsmittel verwendet, sowie alle Zitate als solche kenntlich gemacht zu haben.

Münster, 19. Juni 2015.

Erster Gutachter: PD Dr. Christian Klein-Bösing,
zweiter Gutachter: Prof. Dr. Johannes P. Wessels.

Contents

1 Introduction

Hadronic collisions performed during the last years at the CERN Large Hadron Collider (LHC) reach energies which have never been investigated before. They enable to study the strong interaction as well as other aspects of the Standard Model of Particle Physics and to potentially discover new particles beyond. Since all physicists already have their own, very personal fascinations and motivations about the underlying mechanisms and theories, this beginning will, instead of calling such high perspectives and deep meanings, try to focus more on motivating the following calculations.

The PYTHIA Monte Carlo event generator will be used to explore influences from different mechanisms in jet reconstructions on resulting transverse momentum spectra. In general, computer event generators constitute an important tool to – on the one hand – probe models of particle collisions and the acting mechanisms against measured data and on the other hand, to test detector and analysis frameworks before sufficient measurements of real collisions are available. The latter point implies on the practical side, that event generators need to be checked and tuned to available data to ensure their agreement with physical processes. This work provides checks of PYTHIA calculations to data which have been meausred with ALICE during proton–proton collisions in the LHC at centre-of-mass energies of 2.76 and 7.00 TeV. Steps forwards an integration of next-to-leading order calculations via POWHEG BOX in the PYTHIA showering and fragmentation computations will be shown.

Preparing calculations for the deduction of proton–proton jet spectra at 5.02 TeV from measured data at other energies are part of this thesis. Proton–proton collisions provide the reference for interpretations of proton–lead collisions at the same centre-of-mass energy. Deviations between different collision systems are possible to be seized with the nuclear modification factor, which is sensible to inital-state effects from variant ingoing partonic distributions and to final-state effects which occur after the actual hard collision. In a next step, proton–lead collisions can be seen as a baseline for lead–lead collisions. Presumably not so-called hot matter effects from the creation of a quark-gluon plasma state take place in proton–lead systems, while cold matter effects due to the nuclear environment are expected. As a topic in this thesis, consequences of the rapidity asymmetry in LHC proton–lead collisions will be discussed based on comparisons of calculated jet spectra from symmetric and asymmetric collisions.

As it is typical in particle physics, the convention $c = 1$ is used in the analysis section without explicitly mentioning this.

2 Theoretical Background

2.1 The Standard Model of Particle Physics

The Standard Model (SM) of Particle Physics describes elementary particles and interactions based on symmetries and quantum field theory. The model consists of six quarks (among them *up* and *down* as the main constituents of proton and neutron) and six leptons (including the electron), each with its anti-particle; gauge bosons as mediators of fundamental forces (the gluon in eight colour states, the W bosons, the Z boson and the photon) and the Higgs boson. Three of the known four fundamental interactions (strong interaction, weak and electromagnetic interaction) are part of the model. No significant contradictions between the results of SM calculations and experimental measurements have been observed, mostly up to very high precisions, and particles have been predicted by the model before their experimental observation: the SM can easily be called one of the great achievements of modern physics. On the other hand unexplained observations and indications for "physics beyond the SM" exist, e.g. the gravitational interaction, the matter/antimatter asymmetry and the problem of dark matter and energy in cosmology, the non-zero values and possibly the order of neutrino masses as well as parameters within the model.

2.1.1 Quarks and Leptons

Quarks and leptons are spin-$\frac{1}{2}$ particles (and therefore: *fermions*). Based on group-theoretical reflections and scattering experiments, **six quarks** are considered to be the elementary constituents of hadronic matter. They are grouped in three generations of pairs as listed in tab. 2.1.

Table 2.1: Properties of the six quark flavours [O$^+$14].

Generation	Quark	Mass	El. Charge
I	up (u)	~ 2.3 MeV/c^2	$+2/3\ e$
	down (d)	~ 4.8 MeV/c^2	$-1/3\ e$
II	charm (c)	$\sim 1\,275$ MeV/c^2	$+2/3\ e$
	strange (s)	~ 95 MeV/c^2	$-1/3\ e$
III	top (t)	$\sim 173\,000$ MeV/c^2	$+2/3\ e$
	bottom (b)	$\sim 4\,180$ MeV/c^2	$-1/3\ e$

Up and *down* form an isospin doublet, *charm/strange* and *top/bottom* are characterised by individual flavour quantum numbers. Quarks carry in addition the quantum number *colour*. The states of colour charge are called by convention *red*, *green* and *blue*. Each of these charges can appear with opposite signs (*anti-colour*); colour and same anti-colour cancel out to zero net colour charge. Also the combination of the three colours results in colour neutrality (*white*). Evidence for the existence of colour charge is provided by the occurrence of bound fermionic states of three quarks with equal quantum numbers (e.g. the Δ^{++} particle, composed of three u quarks, all in *spin-up* configuration since coupling to a total spin of 3/2): without an additional quantum number, which is non-equal for the three constituent quarks, this would contradict the Pauli exclusion principle. The bound states of the three lighter quark flavours u, d and s can be projected with respect to isospin and *strangeness* (one of the flavour quantum numbers) in hadron multiplets as representations of the flavour SU(3) symmetry group, namely the baryon decuplet and octet as well as meson nonets [Per00].

Quarks experience all four fundamental interactions. Up to now no free quarks have been observed. This phenomenon is known as *colour confinement*: colour-charged particles, such as quarks, appear only in bound, colour-neutral states. The confinement is mentioned as characteristic of the strong interaction in sec. 2.1.2.

Tab. 2.2 lists the **six fundamental leptons**. They experience gravitation, weak and electromagnetic (except neutrinos, which are electrically uncharged) interaction. The masses of neutrinos are not satisfactorily resolved up to now: initially they were thought to be zero, while the observed *neutrino oscillation* between the three eigenstates implies non-zero masses. In general the cross sections of neutrinos are very small compared the other fermions. In contrast to quarks, the leptons can be observed as free particles.

Table 2.2: Properties of the six leptons [O+14].

Generation	Lepton	Mean lifetime	Mass	El. Charge
I	Electron (e)	$> 4.6 \cdot 10^{26}$ yr	0.511 MeV/c^2	$-e$
	Electron neutrino (ν_e)	(stable)	< 2 eV/c^2	0
II	Muon (μ)	$2.2 \cdot 10^{-6}$ s	106 MeV/c^2	$-e$
	Muon neutrino (ν_μ)	(stable)	< 0.19 MeV/c^2	0
III	Tauon (τ)	$2.9 \cdot 10^{-13}$ s	1777 MeV/c^2	$-e$
	Tauon neutrino (ν_τ)	(stable)	< 18.2 MeV/c^2	0

For each fermion of the SM exists an anti-particle with the same mass as the corresponding particle, but with opposite additive quantum numbers. Consequently a pair of particle and its anti-particle can be created from energy and vice versa. It is up to now an open question wether neutrinos are their own anti-particles (*Majorana fermions*).

2.1.2 Fundamental Interactions and Gauge Bosons

The four fundamental interactions are the strong, the electromagnetic, the weak interaction as well as the gravitation, the first three of which are described within the Standard Model. All four are listed in tab. 2.3 with their gauge bosons. Bosons are, in contrast to fermions, particles with integer spin.

Table 2.3: Properties of the four fundamental interactions and their gauge bosons. The relative strengths are given for two u quarks in a distance of $3 \cdot 10^{-17}$ m [CPE00].

Interaction	Gauge Boson	rel. Strength
Strong	8 Gluons (g)	60
Electromagnetic	Photon (γ)	1
Weak	W^+, W^-, Z^0	10^{-4}
Gravitation	(not discovered)	10^{-41}

Gravitation is up to now not explained within the Standard Model, and it can be neglected in the discussion of collision physics due to by orders lower strength at relevant distances.

The **weak interaction** couples to left-handed leptons and quarks as well as to their right-handed anti-particles. As the name indicates, this interaction is by orders of magnitude weaker than the strong and electromagnetic interaction. The bosons of the weak interaction are the W^+/W^- particles, which also transport electrical charge, and the Z^0 particle, which is electrically neutral. The W^+/W^- are a pair of particle and anti-particle. They can change the flavour of quarks within one duplet and are well known from the β decay, where u and d quark are converted. The Z^0 boson mediates neutral weak currents. The weak interaction acts on small ranges. Due to the high masses of the gauge bosons of the order of GeV/c^2, it has a small coupling: the weak interaction does happen comparatively rarely, as long as processes of the interactions described in the following are possible.

The **electromagnetic interaction** between electrically charged particles is described in quantum electrodynamics. It is mediated by uncharged, massless photons. The effective coupling decreases slightly with distance due to *screening* effects. Screening means an effect of virtual particle/anti-particle pairs, which polarise in the presence of a real charge and so in effect *screen* (diminish) the charge. The screening contribution increases with distance to the real charge, and so the effective charge decreases with distance.

Electromagnetic and weak interaction unify at high momentum transfers and are described mathematically combined in the unified gauge theory of the *electroweak interaction*.

The **strong interaction** is described within quantum chromodynamics. It acts on very small length scales as an attractive force between quarks and gluons (and so induces the formation and establishes the properties of nucleons), mediated by gluons; it acts also as a residual force between close nucleons ("nuclear force", which permits nuclei and determines their stability), described with meson (quark + anti-quark) exchange.

The quantum field theory of the strong interaction arises from the introduction of the three colour charges and the corresponding SU(3) gauge group. The colour SU(3) group has eight linearly independent generators – in a typical representation: the Gell-Mann matrices, which are linearly independent superpositions of colour states and physically the eight gluons of this theory. (A 9^{th} matrix is symmetrical and does not describe the exchange of colour charge.) Thus the spin-1 bosons of the strong interaction carry, in contrast to the gauge bosons of the Abelian electroweak interaction, themselves the charge of "their" interaction; this particularity results in different effects.

Anti-screening of the colour charge should be mentioned in particular. While, as in quantum electrodynamics, screening appears, quantum chromodynamics knows in contrast also anti-screening. This results from self-coupling of gluons in their eight possible colour combinations. The polarisation picture cannot be applied in an equally simple manner as before with screening. As a result of calculations, virtual particles *anti-screen* (augment) the total colour charge. Also this effect increases with distance to the real charge, and so the effective charge increases with distance. Thus screening and anti-screening compete. In quantum chromodynamics, the anti-screening clearly prevails for a theory configuration with up to 16 quark flavours, while 6 are known [Mü13], [RT13]. *Asymptotic freedom* can be identified as an effect: the effective coupling of quarks and gluons at very small distances and high energies is so low that they are nearly free of the strong interaction. In contrast at larger distances and comparable low energies, *confinement* sets in: colour-charged particles cannot be separated. In a simple model, a larger distance of colour-carrying particles results in an increased potential energy and, following this picture, ultimately in the pairwise creation of new particles (*hadronisation*), ensuring colour-neutrality for each newly bound state.

Quantum chromodynamics entails a high mathematical complexity. Solutions can be found with perturbation theory for large momentum transfers [Mü13]. Typically the effective potential is given as

$$V(Q^2) = -\frac{4}{3}\frac{\alpha_s(Q^2)\hbar c}{r} + kr, \tag{2.1}$$

where Q^2 is the momentum transfer, k is a phenomenological constant and where α_s is the coupling of the strong interaction [Per00]. α_S can be obtained directly from perturbative calculations in first order as

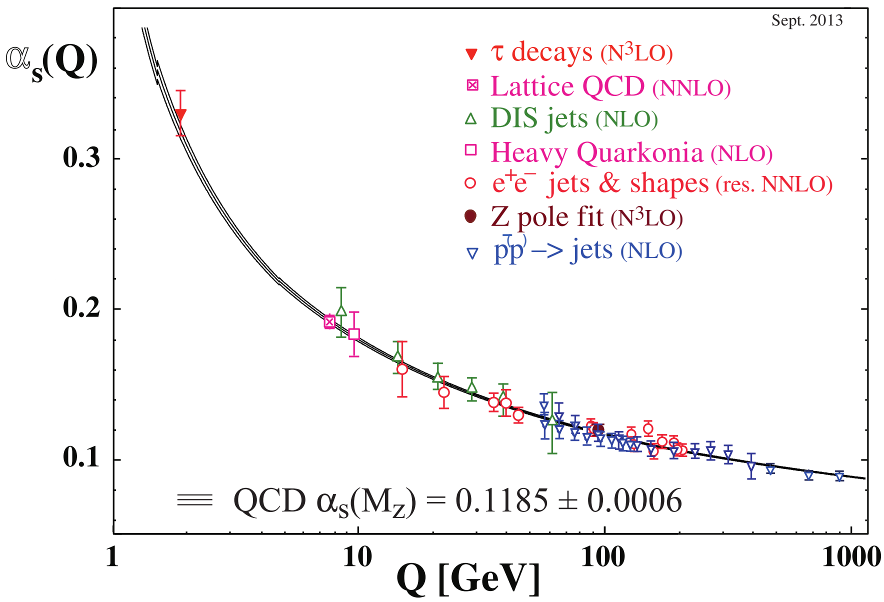

Figure 2.1: Summary of different measurements of α_S as a function of the energy scale Q. This plot is taken from the publication [O+14].

$$\alpha_s(Q^2) = \frac{12\pi}{(11N_c - 2n_f) \cdot \ln(Q^2/\Lambda^2)} = \frac{12\pi}{(33 - 2n_f) \cdot \ln(Q^2/\Lambda^2)}, \tag{2.2}$$

wherein $N_c = 3$ is the number of colours in the theory, n_f the number of available degrees of freedom in quark flavours and Λ the free scaling parameter of QCD [RT13]. Λ can be obtained from measurements of α_S, [RT13] states $\Lambda = 213 \pm 9$ MeV and $\alpha_S(M_{Z^0}) = 0.1184 \pm 0.0007$ with $n_f = 4$ (u, d, s, c). The energy dependence of α_S is shown in fig. 2.1 from measurements and calculations in higher orders.

2.2 Quantum Chromodynamics: Phase Diagram

The expected behaviour of hadronic matter, consisting of strongly interacting particles, can be explored under the use of thermodynamical considerations and in lattice implementations of quantum chromodynamics in the non-perturbative domain. The QCD calculations in a lattice of space and time at zero baryon density (*baryochemical potential* $\mu_B = 0$), as in [Gar13], result typically in a clear change of properties depending on the temperature. This is shown for the energy density ϵ of hadronic matter in fig. 2.2. Above a *critical temperature* T_c, the energy density increases significantly to about 80% of the value as expected for an ideal gas of free particles according to the Stefan-Boltzmann law [Gar13]. Transferred to quarks and gluons, the ideal gas description can be interpreted as a *plasma* state of quasi-free, colour-charged and pointlike quarks and gluons, interacting only weakly above a transition temperature. Thus, the QCD matter *deconfines* in this state above the critical temperature and is not bound in baryons and mesons.

The type of the transition is not fully clarified and depends on the quark masses in the calculations. This can be seen in fig. 2.2, where the case of two massless quarks (approximating *up* and *down*) plus one quark with the *strange* mass shows a smoother transition than in the more simplified cases with two or three massless quarks. Furthermore the transition depends on the baryochemical potential. Classical lattice QCD calculations are restricted to $\mu_B = 0$, while in the last years effort was made to perform extrapolations

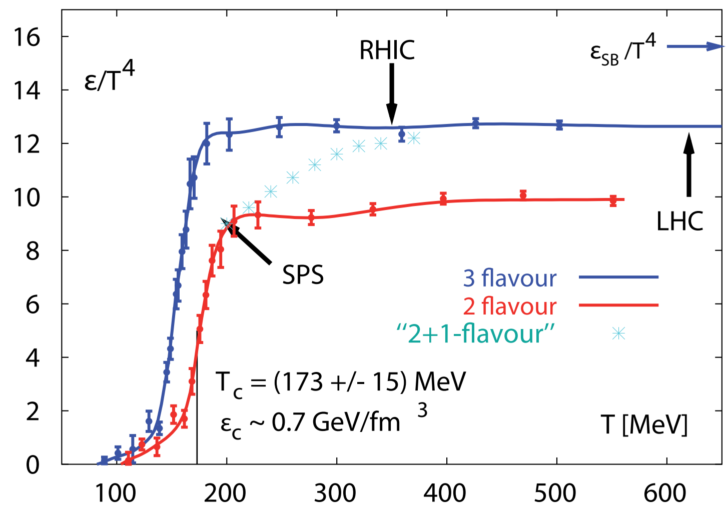

Figure 2.2: Energy density from lattice QCD at $\mu_B = 0$. The calculations in the cited publication are done with two massless quarks (red), with three massless quarks (blue) and with two massless plus one quark with the known strange quark mass (turquoise). The arrow at the upper right indicates the expected energy density for an ideal gas of quarks and gluons. Picture from [Gar13].

to finite μ_B [Fod02]. Some of these calculations show a *critical point* at roughly 3/4 of the baryonic density of normal nuclear matter. Below this point, the transition from the hadronic phase to a Quark-Gluon Plasma is assumed to be a cross-over and not a phase transition. At the critical point a phase transition of 2^{nd} order is assumed, while for higher μ_B a 1^{st} order transition is expected. The transition in the cross-over domain is predicted at temperatures in the range of 150 to 170 MeV, decreasing with μ_B [Gar13].

A sketch of the thermodynamic states of hadronic matter as expected from different calculations according to today's knowledge is shown in fig. 2.3. At very high baryochemical potentials, another transition to a *colour superconducting* state with colour-charged bosonic di-quark pairs similar to the Cooper pairs of electrons in eletrical superconductors is described [Sat10].

The baryochemical potentials in heavy-ion collisions at high energies as in ALICE at CERN (see sec. 3.1) are located below the mentioned critical point. The energy densities are sufficient to reach a thermalised Quark-Gluon Plasma phase, as it is expected from calculations, before the created medium expands and freezes out from the deconfined phase to the known hadronic matter. In contrast and as a possible reference, these conditions are not reached in proton–proton collisions [KB13].

There are different signatures from a Quark-Gluon Plasma in collision processes. According to [Gar13]:

- Thermal radiation: via emerging photons from the created medium, it is possible to apply a thermal interpretation and to infer the temperature of the medium.
- Energy loss of partons/jet quenching: high energetic partons will strongly interact with the created plasma while crossing it. The energy loss should, in a first homogeneous interpretation, obey the proportionalities

$$\Delta E \propto \alpha_S \cdot C_R \cdot \hat{q}(\rho_g) \cdot L^2, \tag{2.3}$$

  where α_S is the strong coupling, C_R the factor expressing the colour charge, $\hat{q}$ the transport coefficient in the plasma depending on the gluon density ρ_g and L the path length through the medium. Thus, e.g. two back-to-back partons with the same momentum from a $2 \to 2$ process will show a different energy loss depending on the individual path length through the medium.

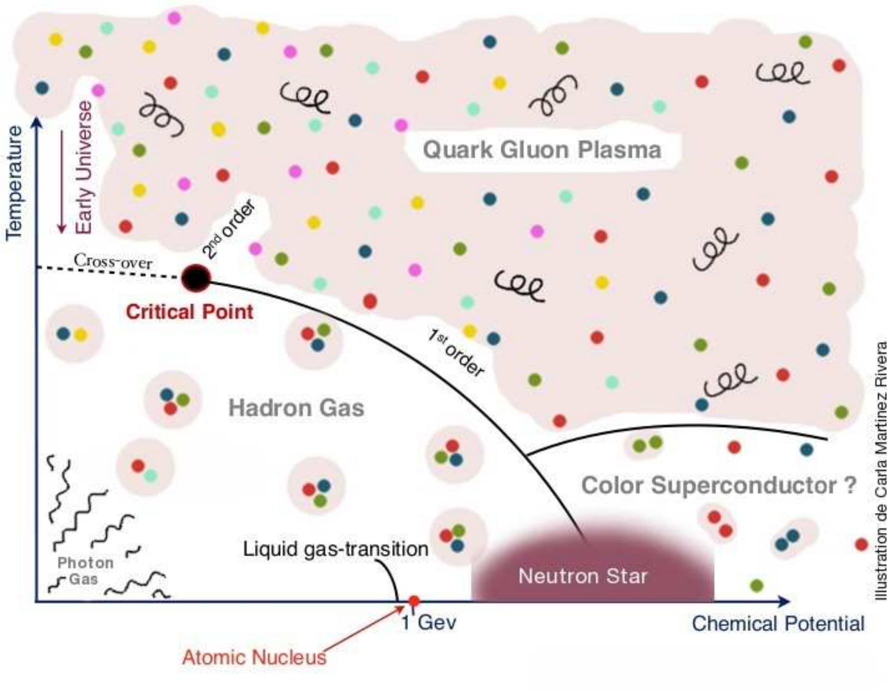

Figure 2.3: Sketch of the hadronic matter phase diagram as considered up to now, from [Gar13].

- Screening of the colour charge: the plasma state implies increased screening due to the high density of colour charges and thus a decrease of the strong-interaction potential for heavy quarks [RT13]. Quarkonia are bound states of heavy quark/anti-quark pairs. Sufficiently high temperatures will dissociate the different states of passing quarkonia at their specific "melting" temperature due to the lowered effective potential, which will thus not only be an indication for the plasma, but also a thermometer, staggered from the available quarkonia states.
- Asymmetric expansion: the geometry of the overlap of the nuclei in heavy-ion collisions can cause a pressure gradient in the expanding plasma and in consequence non-symmetrical distributions of the emerging particles. As an analysis, the particle distributions are decomposed into Fourier components and can be compared with hydrodynamical flow models of the plasma phase. The second Fourier coefficient is associated with the elliptic component of the expansion.

These and further probes exist and are subject to the analysis of heavy-ion collisions compared with collision systems which do not produce comparable thermodynamical conditions and thus presumably no Quark-Gluon Plasma, as e.g. proton–proton, proton–lead and peripheral lead–lead collisions at the LHC.

2.3 Perturbative QCD in Hard Scattering

The coupling α_S of the strong interaction is small in high-energy processes, which enables us to compute cross sections of hadron collisions with perturbation theory. High-momentum transfers imply a short distance and thus allow the approximation of only one parton per nucleon involved in the scattering. For the crossing of the Lorentz-contracted nucleons, a significantly shorter time scale is assumed than for any interaction among the partons of one nucleon (i.e. initial-state effects from the corresponding parton distribution function) – before – as well as for any branching or fragmentation (i.e. the evolution to final hadronic states) – after – the hard parton–parton scattering. Hence, the overall process can be factorised

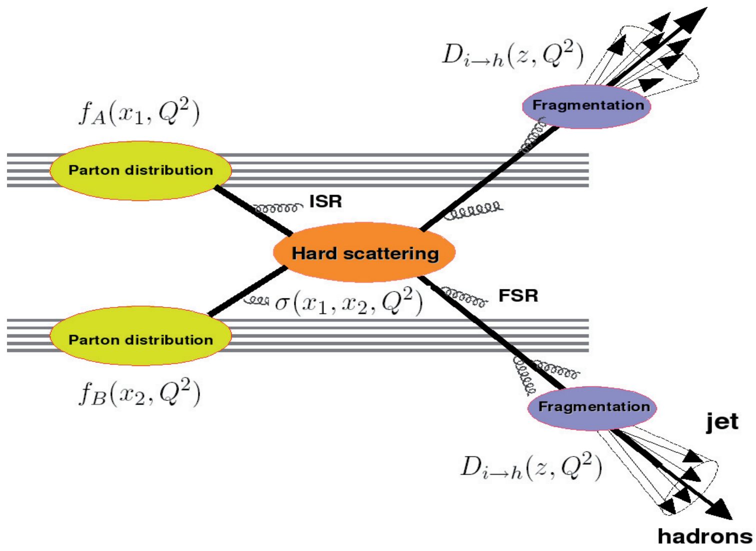

Figure 2.4: Dijet production in the hard collision process of two partons from the nuclei A and B, sketched according to the factorisation into a perturbative hard scattering and further terms as given in eq. 2.4 and discussed in the text. From [d'E09].

into initial-state effects, the hard scattering of partons in effectively "frozen" nuclei and the process of branching and fragmentation [RT13]. The cross section for the production of a hadron h in the scattering of the partons $a+b$ can thus be expressed as given e.g. in [d'E09]:

$$d\sigma^{\text{hard}}_{AB\to h} = f_{a/A}(x_1,Q^2) \otimes f_{b/B}(x_2,Q^2) \otimes d\sigma_{ab\to c}(x_1,x_2,Q^2) \otimes \mathscr{D}_{c\to h}(z,Q^2). \tag{2.4}$$

Here,

- $d\sigma_{ab\to c}(x_1,x_2,Q^2)$ is the cross section for the hard interaction $ab \to c+X$ itself, which can be calculated in perturbation theory.
- $f_{a/A}(x_1,Q^2)$ is a parton distribution function, encoding the probability to find a parton of flavour a with the momentum fraction $x_1 = p_{\text{parton}}/p_{\text{nucleus}}$ in the nucleus A. These functions can be measured in deep inelastic lepton–hadron scattering. On the theoretical side, several approaches exist to calculate PDFs in different orders of perturbation theory.
- $\mathscr{D}_{c\to h}(z,Q^2)$ is the fragmentation function which describes the probability for the outgoing parton c to fragment into a final hadron h with the momentum fraction $z = p_{\text{hadron}}/p_{\text{parton}}$. In a total parton cross section, $\mathscr{D}$ reduces to $\mathscr{D} = \delta(1-z)$ [d'E09]. Also the fragmentation functions can be measured in scattering experiments. Among other main theoretical contributions, the *Lund string model* as described in sec. 3.2 models the fragmentation [RT13].

2.4 Jets in Relativistic Particle Collisions

After the initial collision process of partons from the nuclei of high-energy collisions, the emerging quarks and gluons fragment in subsequent splittings into colour-neutral hadrons. Perturbative showering and the following non-perturbative processes are part of the fragmentation function. Due to the strong scale dependence of the coupling α_S, interactions at high Q^2 are suppressed and the resulting particles are collimated in a small angle around the direction of the primordial parton [KB13], as already sketched in fig. 2.4 about the factorisation of the hard collision. In heavy-ion collisions, the emerging partons cross the produced colour-charged medium, while the whole process of proton–proton collisions is assumed to be realised in QCD vacuum.

Thus, as a typical result, the observed particles of relativistic collisions are collimated into *jets*, which are often described as narrow sprays of particles. In the ideal case, the full momentum of the parton is passed to the resulting jet. An aim of jet analysis is to reconstruct this momentum information of the primordial parton, starting with the mapping of recorded particles to jets. Such reconstruction algorithms are called *jet finders*, whereof the widely used (anti-)k_T algorithm will be a subject of sec. 3.3. Typical jet finders result in jets with closed, non-overlapping areas in the plane around the primary collision vertex. In real collision events with their complex fragmentation functions, the jets do not satisfy the ideal image and cannot be interpreted each as the hadron spray of a single parton [RT13]. Furthermore, the experimentally reconstructed jets in real, densely populated particle distributions depend strongly on the used algorithm and parameters, and thus the jet momenta are also in this respect not unambiguously defined. Altogether, an experimental jet is defined by the way of its reconstruction and is not necessarily congruent with the physical jet from parton showering and fragmentation. Hence a conclusive comparison of jet collections is basically possible only for reconstructions with the same jet finder technique.

2.5 Observations on Jets: Nuclear Modification Factor

Heavy-ion collisions (A+A) can be considered as a process of N_{coll} inelastic, binary nucleon–nucleon collisions. Thus in comparison with proton–proton collisions, the average $\langle N_{\text{coll}} \rangle$ acts as a scaling factor for the yield of outcoming particles in the hard scattering regime (roughly: $p_T > 2$ GeV/c). An often used formulation for the increased parton flux in heavy-ion collisions is the *nuclear overlap function* or *nuclear thickness* $\langle T_{AA} \rangle = \langle N_{\text{coll}} \rangle / \sigma_{\text{inel}}^{\text{pp}}$, where $\sigma_{\text{inel}}^{\text{pp}}$ is the cross section of the hard, inelastic proton–proton scattering [R$^+$12]. T_{AA} and N_{coll} can be determined in *Glauber eikonal calculations* depending on the geometric overlap (*centrality*) of the colliding nuclei [d'E09].

Deviations from this scaling can be registered in the *nuclear modification factor*

$$R_{AA} = \frac{d^2N/dp_T d\eta(A+A)}{\langle T_{AA} \rangle \cdot d^2\sigma/dp_T d\eta(p+p)}, \tag{2.5}$$

where $dN/dp_T(A+A)$ is the momentum-differential particle yield from the A+A collisions. If R_{AA} is smaller than one, this can be interpreted as a consequence of additional energy loss processes of the emerging partons from the A+A collisions in a medium like the Quark-Gluon Plasma. Furthermore R_{AA} is influenced by the shape/steepness of the initial momentum spectra. R_{AA} can be and is often applied to jet yields/spectra. In general, prompt photons from the collision process can be used as a check of the N_{coll} scaling, since photons do not interact with a colour-charged medium and thus are not sensible for final-state effects; their specific R_{AA} should be unity [R$^+$12].

2.6 Energy Scaling of Multiplicity and Total Cross Section

The number of produced particles in a collision is correlated with the initial energy of colliding nucleons. Therefore, the so-called *multiplicity* of the collision scales with the centre-of-mass energy per nucleon pair and, in case of heavy-ion collisions, with the geometrical overlap of the nuclei. The energy dependence

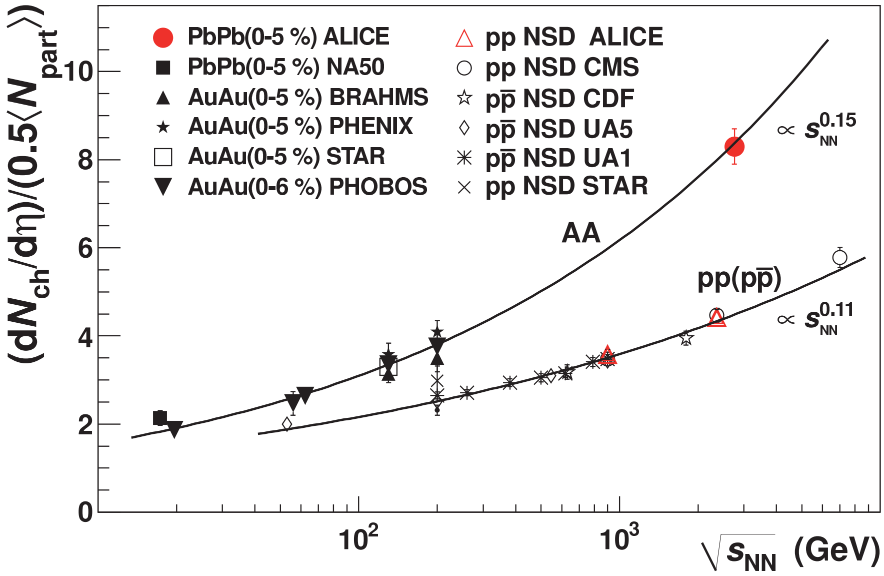

Figure 2.5: Charged particle multiplicities in p+p and in heavy-ion (Au+Au and Pb+Pb) collisions as a function of the energy per binary nucleon collision. The particle yields are normalised to the number of participating nucleon pairs. Particles below a transverse momentum of 50 MeV/c are cut from the yield. From [A+11a].

has been examined from different measurements in [A+11a] for charged particles with a minimum p_T of 50 MeV/c. The result is shown in fig. 2.5. In the heavy-ion case, only the 5% most central (highly overlapping) events are used.

The general expectation is a scaling of the soft processes in a heavy-ion collision with N_{part}, i.e. the number of participating nucleons, and a scaling of the hard processes with N_{coll}, the number of binary collisions. Since the total particle production is clearly dominated by low-momentum particles, the overall multiplicity should scale predominantly with the number of participant nucleons. Hence the charged particle yields in the figure have been normalised with the participant pairs $N_{part}/2$. $\langle N_{part} \rangle$ of the Pb+Pb collisions has been determined in Glauber calculations to 381 ± 18.

The resulting energy dependence differs between p+p and A+A collisions: shown in the figure are curves $\propto s_{NN}^{0.11}$ covering the p+p points and $\propto s_{NN}^{0.15}$ covering the A+A points [A+11a].

Furthermore, the total and elastic cross sections of p+p collisions are shown in fig. 2.6 over a wide range of $\sqrt{s_{NN}}$. The inelastic contributions clearly dominate above a centre-of-mass energy of 3 GeV. The cross section depends only weakly on the collision energy in the inelastic domain.

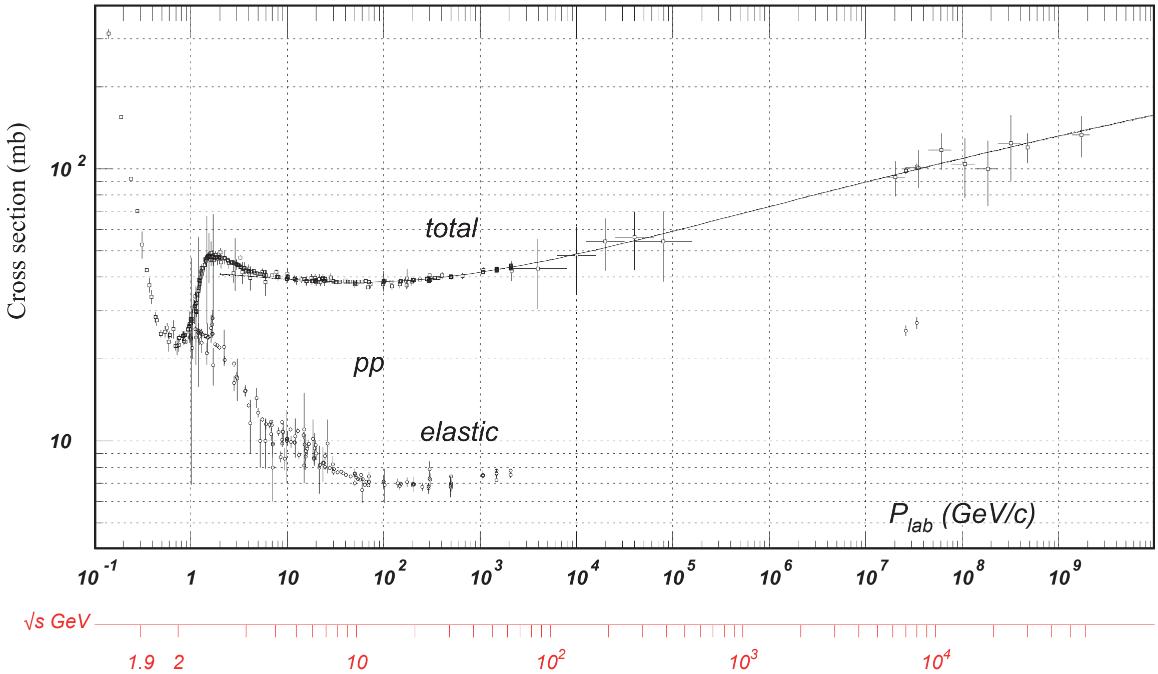

Figure 2.6: Total energy dependence of the total cross section and its elastic part in p+p collisions. From [O+14].

3 Experimental Setup and Methods of Analysis

3.1 A Large Ion Collider Experiment at the Large Hadron Collider

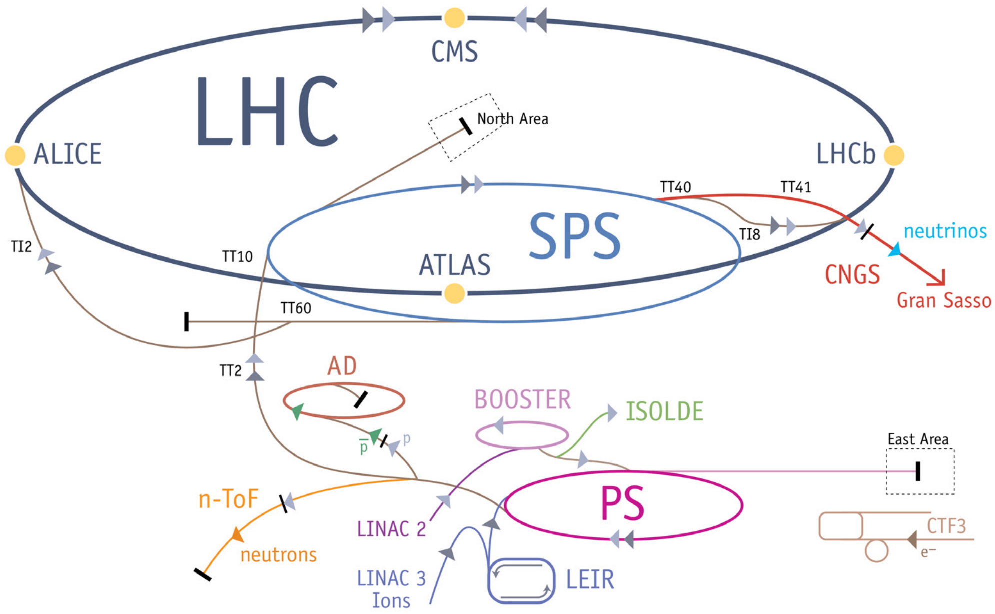

Figure 3.1: Conceptional drawing of the accelerator complex at CERN. The main experiments ALICE, ATLAS, CMS and LHCb at the LHC ring are included with yellow markers. The first pre-accelerators in the used chain are LINAC 2 for protons and LINAC 3 for lead ions. From [Lef08].

A Large Ion Collider Experiment (ALICE) is a detector experiment located at one of the collision points of the *Large Hadron Collider* (LHC) at the *European Organization for Nuclear Research* (CERN) in Geneva. The LHC ring, various pre-accelerators and the main experiments are sketched in fig. 3.1. The LHC can accelerate protons as well as heavy-ions contra-rotating in its two beam pipes. The beams consist of bunches of the accelerated particles. In the first run period from 2009 to 2013, the LHC provided the experiments at its collision points with proton–proton collisions at centre-of-mass energies up to $\sqrt{s} = 8$ TeV, lead–lead collisions of $^{208}\mathrm{Pb}^{82+}$ ions at $\sqrt{s_{\mathrm{NN}}} = 2.76$ TeV and proton–lead collisions at $\sqrt{s_{\mathrm{NN}}} = 5.02$ TeV. The designed peak luminosity of the LHC is 10^{34} cm^{-2}s^{-1} for proton–proton runs, while ALICE is operated at lower luminosities of 10^{30} cm^{-2}s^{-1} by displacing the proton beams. In the first LHC run, a reduced luminosity in ALICE was especially reached by choosing a filling pattern of the LHC with a lower number of colliding and less focused bunches in the corresponding interaction point [EB08]. The maximum lead–lead luminosity in ALICE is 10^{27} cm^{-2}s^{-1}, the proton–lead runs reached about $8 \cdot 10^{25}$ cm^{-2}s^{-1} [A$^+$12b]. ALICE is capable to record the high multiplicities of heavy-ion collisions [A$^+$08]. A glimpse of the recorded events in the first LHC run is provided in fig. 3.4 in the end of this section.

ALICE consists of various detector systems as schematically shown in fig. 3.2. The central part of the experiment is embedded in a large solenoid magnet (L3), which provides a magnetic field of 0.5 T with the

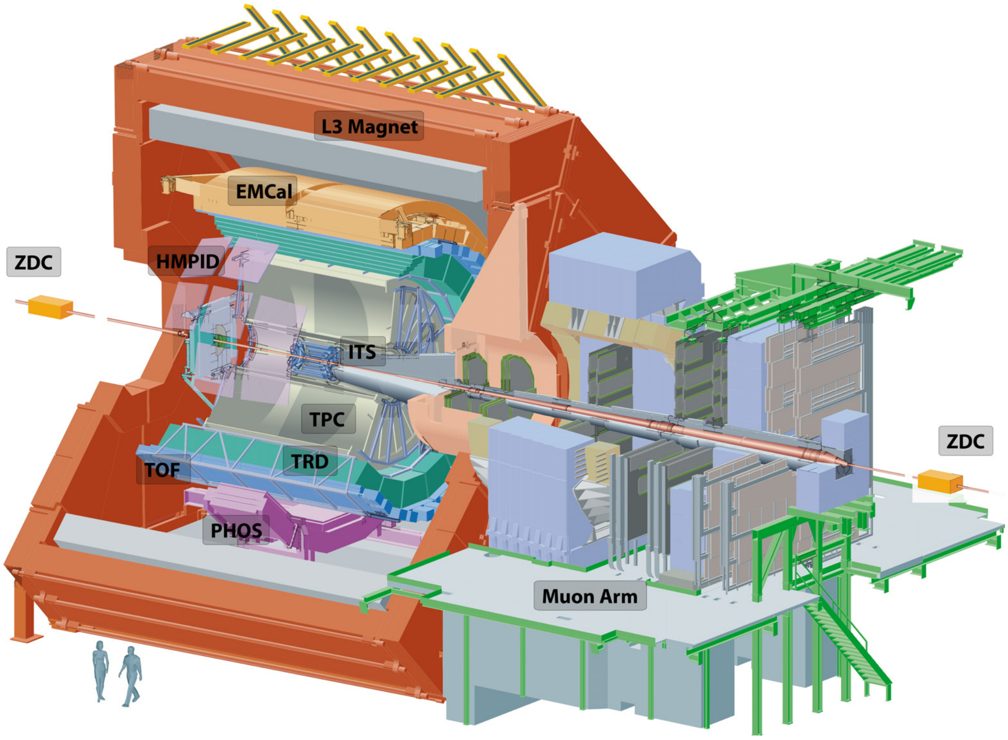

Figure 3.2: Schematic view of ALICE at CERN. The detector subsystems for particle tracking, identification and calorimetry are installed inside the red L3 magnet, often named the “central barrel”. The right side shows a specialised muon spectrometer. Modified from [A+08]. See there for details.

aim to deflect all electrically charged particles and thus allows to measure their momenta. In principle, the subdetectors can be divided in tracking detectors for charged particles and calorimetric detectors, which are sensible also to electrically neutral particles. The ALICE systems (Inner Tracking System, Time Projection Chamber and Transition Radition Detector as important contributors) are able to track charged particles and measure their momenta from some tens of MeV/c up to over 100 GeV/c. Particle identification is performed with manifold methods: by analysing the specific ionisation energy loss, the time-of-flight, transition and Cherenkov radiation, with electromagnetic calorimetry, muon filters and topological decay reconstruction [A+08].

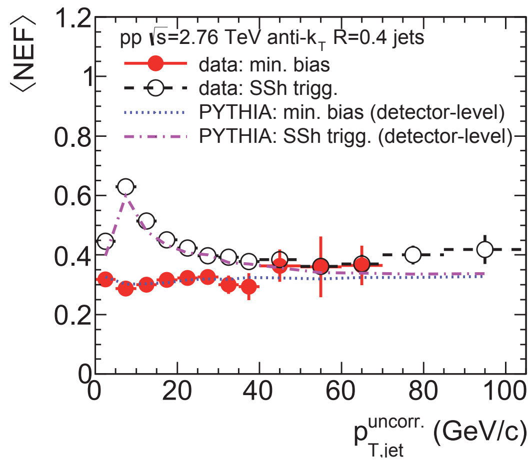

Figure 3.3: Example of the mean Neutral Energy Fraction (NEF) of jets from proton–proton collisions at a centre-of-mass energy of 2.76 TeV in ALICE, recorded with minimum bias and with a “Single Shower” trigger implementation requiring a minimum energy deposition in the EMCal. From [A+14b].

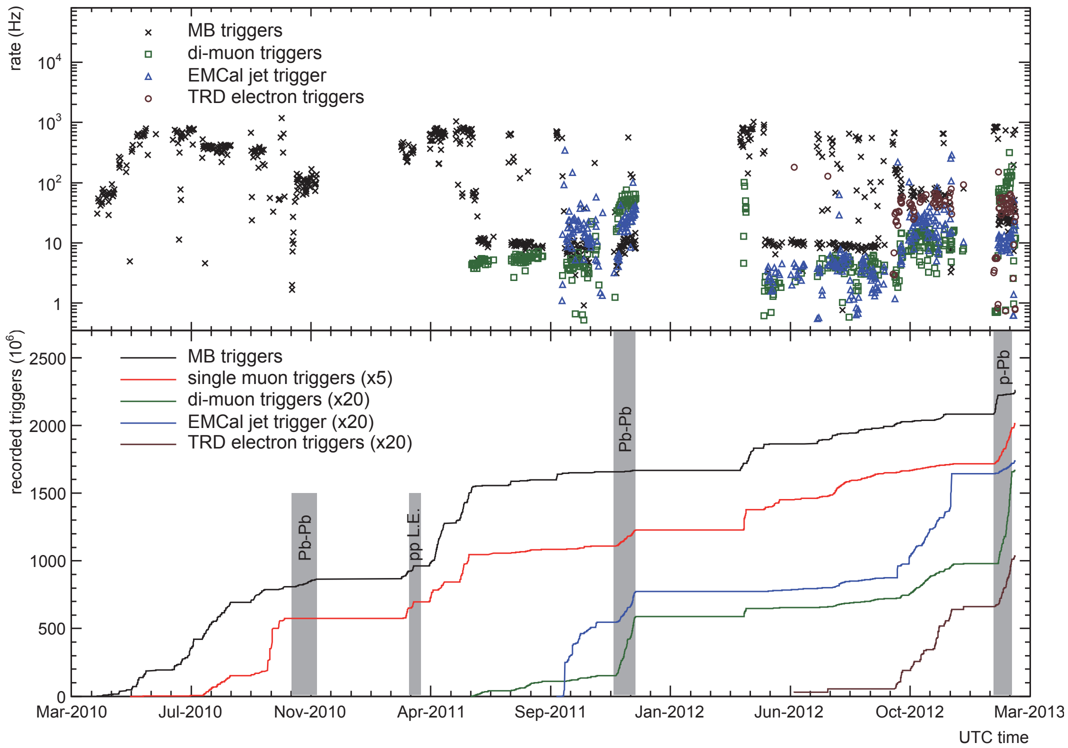

Figure 3.4: Instantaneous rate (top) and integrated number of observed events (bottom) during the first LHC run period from different trigger systems in ALICE; the curves in the lower plot are scaled as declared in the legend. LHC runs with heavy-ions (Pb+Pb and p+Pb collisions) instead of protons only and proton runs at lower energies are indicated with grey bands. From [A$^+$14b]. See there for the trigger definitions.

On the other hand, the calorimetric detectors (Photon Spectrometer, Electromagnetic Calorimeter) are able to resolve the full spectra of emitted particles including the electrically neutral fraction. An example of the *Neutral Energy Fraction* (NEF) in jets from proton–proton collisions at 2.76 TeV as published in [A$^+$14b] from ALICE data and Monte Carlo computer calculations is shown in fig. 3.3. Due to the lower geometrical acceptance of the calorimeters (e.g. EMCal covers an azimuthal range $\Delta\varphi = 107°$ for $|\eta| < 0.7$ in contrast to the full azimuth of Inner Tracking System, Time Projection Chamber and Transition Radiation Detector [A$^+$08]), some analyses use only electrically charged particles. Results obtained with jet reconstructions from charged particles only ("charged jets") can be transferred with respect to many of their properties to "full jet" reconstructions which include the full particle collection.

3.2 Computer Event Generators

3.2.1 PYTHIA

PYTHIA is a computer program for the generation of collision events between elementary particles on purely simulative level, based on a Monte Carlo process. It is intended to deliver the complete outgoing particle distributions from high-energy lepton–lepton and hadron–hadron collisions with centre-of-mass energies greater than 10 GeV, where resonance effects do not significantly contribute. PYTHIA combines perturbative calculations of the initial few-body system in a hard scattering which can be derived from theory, with phenomenological models of the complex evolution to a multiparticle final state. The perturbative calculations are formulated in leading order (LO), also the non-perturbative models are intended

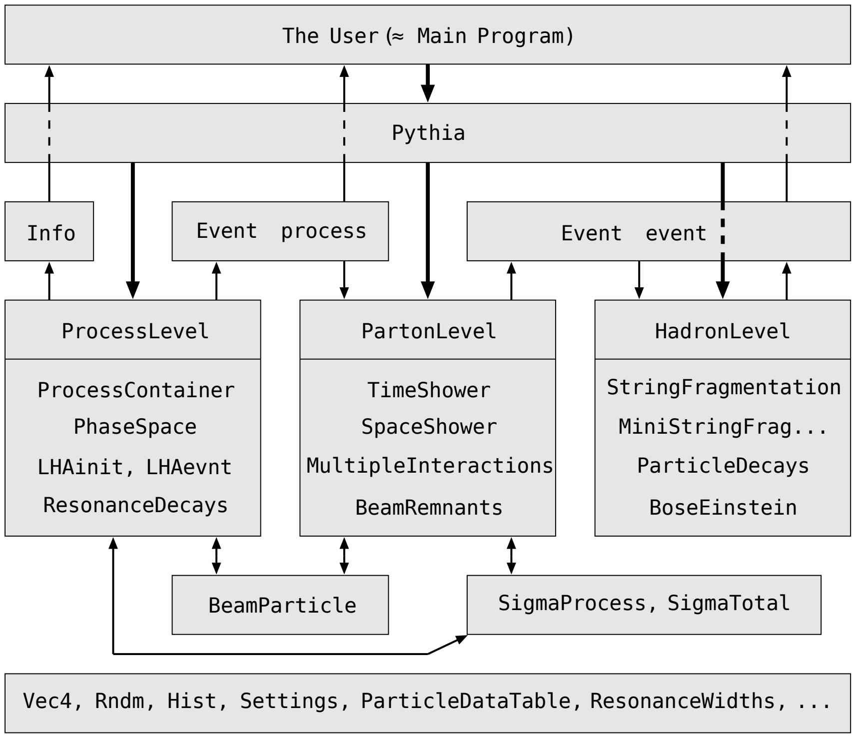

Figure 3.5: The main classes in PYTHIA in a simplified chart. The thick arrows indicate the flow of commands for different physics tasks, while the thin arrows show the flow of informations between such tasks. The bottom box contains common tools available in all tasks. From [SMS07].

to reach LO precision. Some next-to-leading order (NLO) corrections are included. All outgoing particles are produced in vacuum; interactions with detector material and further detector effects are not included in PYTHIA. The structure of the program can roughly be divided in the calculation of the hard process, secondly the activity on the partonic level, including initial- as well as final-state radiation, multiple parton interactions and beam remnants and thirdly the hadronisation of this partonic configuration. The program structure in fig. 3.5 shows the corresponding three main classes `ProcessLevel`, `PartonLevel` and `HadronLevel` [SMS07], [SAC$^+$14]. A more detailed description of the mechanisms is available in [SAC$^+$14]:

– The **hard-process** part provides a variety of physical processes. The hard-QCD section calculates $2 \to 2$ and $2 \to 1$ processes, with also few $2 \to 3$ processes available. Other sections implement electroweak reactions like prompt photon production, production of single $\gamma^*/Z/W^+/W^-$ and weak boson pairs, production of quarkonia like charmonium or bottomonium in different states, top quark production and further processes. Also "new physics" like Supersymmetry particle production, 4^{th} generation physics and new gauge boson reactions are available. The default set of parton distribution functions in PYTHIA 8.1 is CTEQ 5L, but other PDF sets can be chosen separately for the hard interaction and subsequent processes [SMS07]. Also preset tunings of PYTHIA use different PDFs.

  The hard-process part can be overridden by the input from an external hard-process generator via LHE files ("Les Houches Event" format) which transport a list of the in- and outgoing particles of the calculated processes including, i.a. their momentum, energy, colour and spin informations [ABB$^+$06].

– **Parton showering** processes are calculated based on branching probabilities of dipole-style splitting kernels. Beginning with PYTHIA 8.1, the entire perturbative contributions to showering (initial- as well as final-state radiation and multiple parton–parton interactions) are interleaved into one sequence ordered by decreasing p_{T} [SMS07]. For final-state radiation, this corresponds to a timelike evolution of the shower forwards in physical time and thus is implemented in the `TimeShower` class. Here, a parton can branch with a certain probability in pairs of daughter partons. In contrast, initial-state radiation corresponds in the decreasing-p_T description to a spacelike evolution backwards in time and thus is implemented in the `SpaceShower` class, where evolving partons become unresolved in $2 \to 1$ processes with one sister parton into one new mother parton. The overall strength of intial- and final-state radiation directly depends on the effective value of $\alpha_S(M_Z)$, which can be set separately for both radiation types. The recommendation in PYTHIA is to set $\alpha_S(M_Z)$ to a higher value than the general 0.1184 [RT13], in order to take different LO and NLO corrections into account. The values of $\alpha_S^{\mathrm{PYTHIA}}(M_Z)$ in different tunings of the program are given in sec. 4.2.5.

– **Multiple parton–parton interactions** occur due to the composite structure of colliding hadrons and are relevant for the soft underlying contributions to the total event. The overall parton densities for the multiple interaction calculations are rescaled after the first hard scattering. For the multiple interactions, partonic $2 \to 2$ QCD scatterings are taken into account as well as e.g. again the production of prompt photons and quarkonia.

– The first hard scattering and multiple interactions of partons can cause complicated **beam remnants**, which are treated in a model of the remaining colour-charge structure. Colour reconnection as an influence on the colour flow of multiple parton interactions can be considered here.

– The **hadronisation** in PYTHIA is based on the *Lund String fragmentation framework*. Since QCD is not solved in the corresponding domain of lower energies, alternative models need to be applied. The Lund String model is derived from a simple linear confinement picture, as mentioned in sec. 2.1.2: the potential energy in a colour dipole field between two charges increases linearly with the separation of the $q\bar{q}$ pair until the energy in this colour flux is sufficient to create a new $q'\bar{q}'$ pair, which enables the whole system to split in two pairs $q\bar{q}'$ and $q'\bar{q}$. Arguments to use this model are found with hadron spectroscopy and in lattice QCD studies. The production of new quarks is calculated in accordance with a quantum mechanical tunneling process. The lighter quark flavours u, d and s are preferred in this production. A simple hadronisation process with several splittings is sketched in fig. 3.6. The fragmentation model in PYTHIA also takes more complicated structures like hadronising $q\bar{q}g$ formations into account. Further details can be found in [SAC+14].

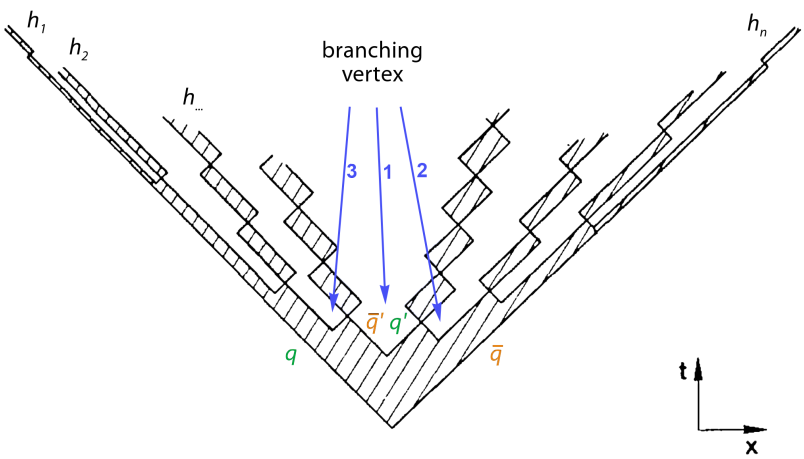

Figure 3.6: One-dimensional and strongly simplified sketch of a hadronisation process, starting from the quark pair $q\bar{q}$. The shaded areas mark regions of colour coherence. The first new quark pair, which appears in the splitting vertex "1", is labelled as $q'\bar{q}'$. Also the following two vertices are marked with arrows. The process ends with the hadrons h_1 to h_n. The transverse momenta of the produced particles are calculated in accordance with a quantum mechanical tunneling process for the production of these pairs. Modified from [AGI+83].

The models applied in the different program classes can be tuned with respect to several parameters. Due to the partly phenomenological character of these models, most of their parameters need to be adjusted in comparison with data from measured collisions. Such tunings have been performed in many studies during the development of PYTHIA, initially based on measurements of leptonic electron–positron collisions at the CERN LEP, later on proton–antiproton collisions at the Tevatron and latterly in comparison with measurements at the different LHC experiments. The overall energy scaling is explicitly named as source of uncertainties in calibrations [SCD+15]. While a variety of tunable parameters exists, the basic settings as the effective values of α_S in the different program sections are the most influential ones [SC10]. The predefined tunes of PYTHIA 8.175 are presented in detail in sec. 4.2.5.

3.2.2 POWHEG BOX

"Positive Weight Hardest Emission Generator" (POWHEG) defines a method to perform perturbative QCD calculations of hard hadron–hadron scatterings up to next-to-leading order (NLO). The POWHEG BOX framework is an implementation of this method, which enables to interface the calculated NLO emissions to Shower Monte Carlo programs (SMC) such as HERWIG or PYTHIA, with the aim to generate final hadronic collision events with this process chain.

Many SMC programs already implement some approximate NLO corrections as e.g. gluon radiation in the final state. Consequently, MC@NLO interfacing can lead to a doublecounting of these effects. In early implementations, the doublecounting is treated with subtracting approximate (SMC-sided) NLO corrections without further matching from the exact NLO cross section before the interfacing is done. Since the difference is not necessarily positive, this procedure entails about 10 to 15% of the total events to be negative-weighted. The POWHEG method ensures all weights to be positive by generating the hardest radiation first and defining a matched hardness criterion, which is typically about 2 GeV. Emissions calculated in the POWHEG are required to be above the chosen threshold. The succeeding p_T-ordered SMC program vetoes in contrast all emissions above the threshold. The POWHEG and the SMC program should be set to use the same parton distribution functions [SCD+15], [Nas04], [FNO07], [ANO+10].

The interfacing of POWHEG calculations to a SMC program is typically realised via LHE files for particle listing [ABB+06]. This is done for the analysis in chapter 5, using POWHEG BOX data and PYTHIA, where the NLO calculations replace the LO hard process generation.

3.3 Jet Finders

The purpose of jet finder algorithms to deduce the original momentum information of emitted partons by reverting the showering and hadronisation processes from a measured (or calculated) particle collection and general differences between the theoretically expected and the reconstructed jets have been mentioned in sec. 2.4 and 2.5. In the following, the widely used k_T and anti-k_T jet finders will be depicted as examples of such real reconstruction algorithms.

3.3.1 k_T and anti-k_T algorithm

The k_T and the anti-k_T algorithms define recombinatorial procedures which subsequentially cluster the particles of a given event to jets until, separately for each jet, a completion criterion is fulfilled. In the end, all particles of the clustered event are assigned to exactly one jet. A distance measure between two objects i and j in the η-φ plane around the collision vertex is essential for any jet definition:

$$R_{ij} = (\eta_i - \eta_j)^2 + (\varphi_i - \varphi_j)^2. \tag{3.1}$$

The k_T algorithms use in addition the following momentum-weighted distance measures:

$$d_{ij} = min(p_{T,i}^{2p}, p_{T,j}^{2p}) \cdot \left(\frac{R_{ij}}{R}\right)^2 \text{ and} \tag{3.2}$$

$$d_{iB} = p_{T,i}^{2p}. \tag{3.3}$$

R is the free *jet resolution parameter* and can be considered as a target radius for the reconstructed jets. The parameter p is 1 for the k_T algorithm and -1 for the anti-k_T algorithm [CSS11].

The full formulation for the algorithm is, according to [CSS11]:

1. Calculate the distance d_{ij} as given in eq. 3.2 for each pair of particles i, j in the event. Also calculate the beam distance d_{iB} as given in eq. 3.3 for each particle i.
2. Choose the minimum value out of all d_{ij} and d_{iB}. If this is a d_{ij}: merge i and j to a new single element. If this is a d_{iB}: declare the element i a finished jet. Remove it from the list of elements.
3. Repeat from step 1 until no elements are left.

Obviously the k_T algorithm begins the clustering with the smallest particle momenta, while anti-k_T starts to cluster around the hardest particles. Typically anti-k_T ends with geometrically more circular jets and is often preferred for the main jet analysis. k_T is preferred for background analyses due to stronger sensitivity of its determined jet areas to soft particles. Both variants of the algorithm fulfil per definitionem *infrared and collinear safety*: neither will additional soft (infrared) particles change the resulting jet collection by merging former separate jets nor will collinear splittings cause the resulting jet to split [CSS11].

It is essential for jet finder algorithms to define how momenta and directions of combined elements are determined. This definition is in case of the FastJet framework [CSS11] given, among others, in the *recombination schemes E* and p_T. The E scheme simply adds the four-momenta of the elements to merge. In the p_T scheme the combination of the 4-momenta p_i and p_j to p_r is defined as:

$$p_{T,r} = p_{T,i} + p_{T,j}, \tag{3.4a}$$

$$\varphi_r = \frac{w_i\varphi_i + w_j\varphi_j}{w_i + w_j} \text{ and} \tag{3.4b}$$

$$\eta_r = \frac{w_i\eta_i + w_j\eta_j}{w_i + w_j} \tag{3.4c}$$

with the weight $w = p_\mathrm{T}$. The p_T scheme rescales each ingoing energy value proportional to the norm of the 3-momentum in order to make the initial momenta massless. The mentioned recombination schemes are not invariant under longitudinal Lorentz boosts when particles with non-zero masses are involved. FastJet defines in addition a boost-invariant p_T scheme ("BIpt") without the preceding energy rescaling, which then consequentially shows mass-afflicted momenta.

3.3.2 Determination of Jet Areas

Within the FastJet package it is possible to determine the area of jets in different ways. *Area* is to be understood here as a measure of the region occupied by a jet in the η-φ plane. The methods offered by FastJet are [CSS11]:

- *Active areas*: A large quantity of massless and extremely soft *ghost* particles with a mean p_{T} of the order of 10^{-100} GeV/c is added to the event, which is analysed by the jet finder algorithm. The ghosts are distributed homogeneously in the analysed part of the η-φ plane and participate in the clustering process. Infrared-safe algorithms are by definition invariant under the addition of sufficiently soft particles. Due to the uniform distribution of the ghosts, their number in a previous clustered jet is proportional to the area of this jet.
- *Passive areas*: Only one ghost is placed randomly in an event and participates in the clustering. The jet finding is repeated many times with different uniformly distributed positions of the single ghost, until the whole process converges to a probability of containing the ghost for each jet. This probability is proportional to the jet area. Due to the large number of repetitions, this method is usually the slowest in terms of CPU time.
- *Voronoi areas*: To each single particle in the analysed surface, an area is assigned by the purely geometrical construction of Voronoi diagrams. In FastJet this is done "with the help of Fortune" [For87], who proposed an efficient Voronoi algorithm. The jet area is the sum of all Voronoi cells in a jet. This method is very fast for events with a large number of participants.

As a variant, the *active areas with explicit ghosts* type includes explicitly all added ghosts up to the final jet constituents. While hard jets are identical to those of the basic active method, this "explicit" type delivers also very soft "pure ghost" jets. To cluster such ghost jets is beneficial in sparsely populated events in order to avoid the overestimation of areas of real physical jets [CRS^{+}10].

The difference between the active and the passive area definition follows from understanding the ghosts in the role of background particles. The "active" method provides areas in the sense of a diffuse and more regular background, while the "passive" areas are related to point-like background structures. Actually, the areas of all three main definitions should converge for dense particle distributions.

4 PYTHIA Event Generation and Jet Energy Scaling

4.1 General Settings

The main calculations presented in this chapter are done with the PYTHIA 8.175 event generator that is described in sec. 3.2.1. The configuration was set for proton–proton collisions with centre-of-mass energies of 2.76, 5.02 and 7.00 TeV, as reached in the Large Hadron Collider for proton–proton (2.76 and 7.00 TeV), proton–lead (5.02 TeV) and lead–lead (2.76 TeV) collisions. In order to obtain high statistics over a broad p_{T} scale, the calculations have been divided into 20 single ranges of $\hat{p}_{\mathrm{T}}$, the transverse momentum transfer in the hard process, beginning with a bin from 5 to 7 TeV and up to a last bin with $\hat{p}_{\mathrm{T}}$ above 180 GeV, each bin containing 50000 collision events. After scaling the resulting spectra with the specific weight corresponding to the cross section of their $\hat{p}_{\mathrm{T}}$ range, these components can be summed to a complete picture of the set collision process. Since the calculations for every bin consist of the same number of collision events, the statistical quality reaches a higher homogeneity in p_{T}, independently of the shape of the spectrum, by using this splitting technique. An example of used weights, namely the cross sections for the corresponding $\hat{p}_{\mathrm{T}}$ bin as determined in PYTHIA with the function `sigmaGen`, is shown in fig. 4.1. In addition, the calculations for each given configuration have been repeated 20 times with different random number seeds in the PYTHIA Monte Carlo process to gain higher statistics and to enable parallelisation of the calculations to multiple CPU cores.

Furthermore the resulting particle compositions of each PYTHIA event have been passed to the FastJet package [CSS11] to cluster jets with the (anti-)k_{T} algorithm (defintion in sec. 3.3.1). Used resolution parameters R are 0.2 and 0.4. The term "charged jets" is in the following, as usual, to be understood as jets which are constructed only from the electrically charged particles of an event. While PYTHIA enables the examination of the complete particle production irrespectively of type, momentum and the direction of emission, real detectors are bound to their physical possibilities. The main detectors for charged particle tracking in ALICE, the *Inner Tracking System* (ITS) and the *Time Projection Chamber* (TPC), cover a pseudorapidity range of $|\eta| < 0.9$ in full azimuth of 2π [A$^+$08]. (The inner layer of the ITS covers a larger η range, also the TPC can reconstruct a larger η range, but not with full momentum resolution due to reduced track lengths.) The available p_{T} range of reconstructions and the geometrical conditions are simulated here by requiring a minimum p_{T} of 0.15 GeV for each final particle and applying an acceptance cut of $|\eta| < 0.9$ on the generated collection. In addition, neutrinos are rejected for further analysis. For reconstructed jets an additional requirement is from simple geometric reasons $|\eta| < (0.9 - R)$, which is fulfilled here by using $|\eta| < 0.5$ for all jet collections, if no variant range is defined. The usage of the same η range for all jet reconstructions independently of its resolution parameter R ensures full comparability of these reconstructions.

If not explicitly mentioned, the boost-invariant p_{T} recombination scheme of FastJet has been used with massless particles (by defining $E = p$) to calculate the jet momenta after clustering their participants.

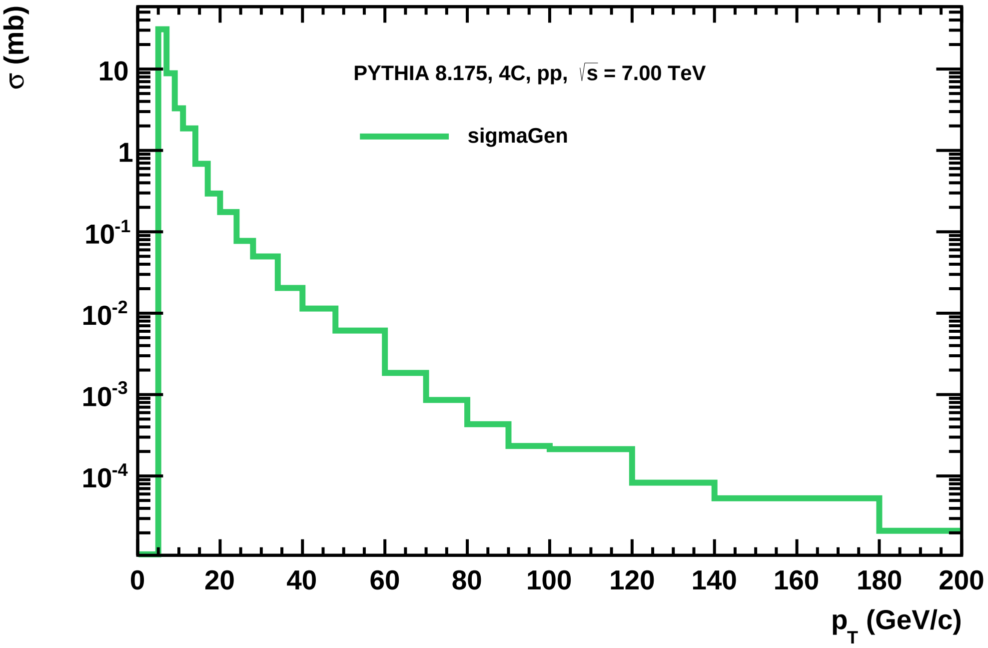

Figure 4.1: Example for the cross sections of single $\hat{p}_T$ bins from the calculation of a pp collision at 7 TeV in PYTHIA with its default tune 4C. The values are determined with the `pythia.info::sigmaGen` function. The shown cross sections are multiplied to the single spectra of the corresponding $\hat{p}_T$ ranges before these components are summed to a complete spectrum.

4.2 Contributions to Systematic Uncertainties in Jet Spectra

4.2.1 Trigger Condition in PYTHIA calculations

PYTHIA calculations are used in analyses of the ALICE collaboration for instance in detector response determinations, which are performed by applying a detector simulation on generated events and comparing the resulting jets to the jet spectrum from the same, but unmodified event (ensuring geometrical matching of the jets in this comparison). The known detector response enables to correct jet spectra from measured data to the particle level. For the jet R_{pPb} in the ALICE collaboration which is published in [A$^+$15], a full detector simulation is performed with PYTHIA-generated events. Also a jet spectrum at 2.76 TeV from the ALICE collaboration [A$^+$13b] corrects to the particle level by weighting every bin of the jet spectrum with

$$c(p_T) = \frac{d\sigma^{\text{particle}}_{\text{PYTHIA}}(p_T)/dp_T}{d\sigma^{\text{detector}}_{\text{PYTHIA}}(p_T)/dp_T}. \tag{4.1}$$

With the general aim to reduce the necessary storage size, filters are applied on the resulting Monte Carlo data in some projects. In the following, a "software trigger" is thus probed for its effects on a jet spectrum. The applied condition is: a generated event is considered in the analysis if, and only if this event contains at least one full jet with $p_T > 10$ GeV within $|\eta| < 1.5$. The anti-k_T clustering for this check is done with a resolution parameter of $R = 1$. In case this condition is set in calculations with different jet clustering settings, e.g. the reconstruction of jets from charged particles only and with a "smaller" resolution parameter R, any effects on jets above the trigger threshold should be excluded. This exclusion is shown in fig. 4.2 using the ratio of a triggered over the unfiltered jet spectrum for charged jets with $R = 0.4$: charged jets above the threshold p_T used in the trigger with its full jet condition are not affected. This result is stable against changes of the initial collision energy and/or the jet finder resolution parameter.

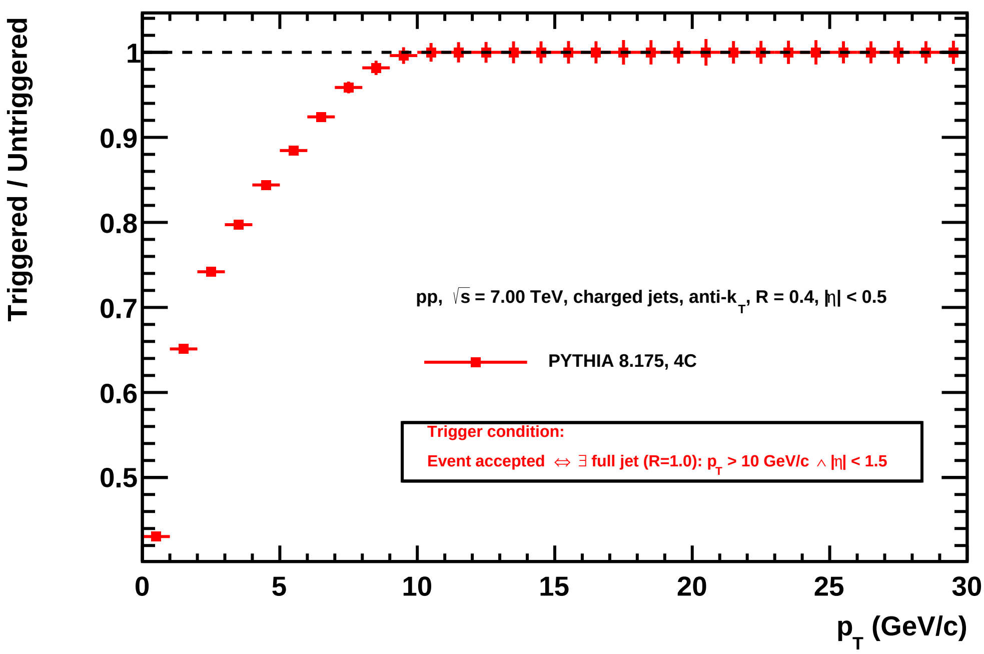

Figure 4.2: Test of the effect of a "software trigger" in the calculation of jet spectra.

4.2.2 Jet Recombination Schemes

Different recombination schemes are in general described in sec. 3.3.1. The common choice for the analysis of ALICE data is the "boost-invariant" p_{T} scheme, while the particle mass is typically defined to be zero by setting $E = p$ for each particle. To investigate the influence of different recombination schemes in the calculation chain of jet spectra, spectra from 7.00 TeV p+p collisions have been determined also with the boost-invariant p_{T} scheme without the described manual energy rescaling and with the p_{T} scheme. The latter mentioned p_{T} scheme includes a preprocessing in the FastJet algorithm, which rescales the energy to be equal to the 3-momentum and so results in massless particles in the same way as manually done in the "boost-invariant" p_{T} scheme.

All jet clusterings are done on the basis of the same PYTHIA particle generation in order to avoid influence of statistical fluctuations.

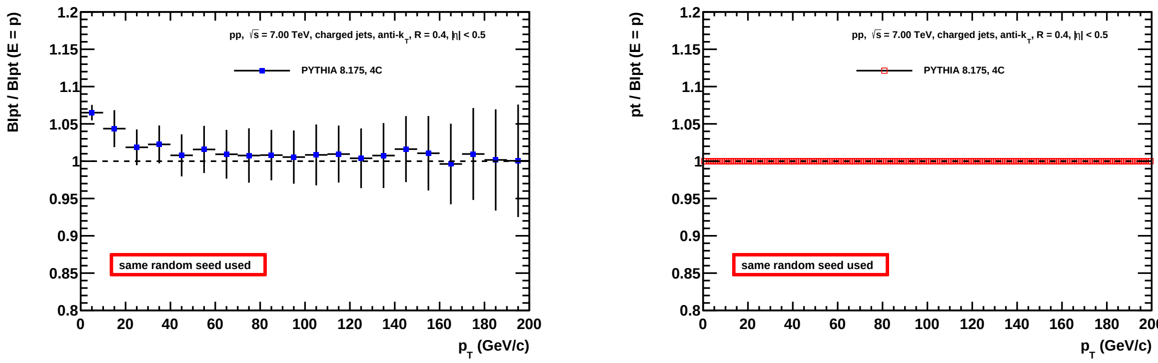

Figure 4.3: Ratios of charged jet spectra at 7.00 TeV, clustered in anti-k_T, $R = 0.4$, with different recombination schemes. See text for the descriptions of the schemes. All used spectra are clustered from the same PYTHIA generation in PYTHIA 8.175 with its default tune 4C.

The boost-invariant p_{T} scheme without energy rescaling results (see fig. 4.3, left) in a jet spectrum very similar, but not identical to the "boost-invariant" p_{T} scheme with manual energy rescaling. The main deviations can be seen in the low-p_{T} region, where the difference between energy and momentum is significant. Low-p_{T} jets are governed by pions ($m_{\pi^{\pm}} = 139.6$ MeV) [R^{+}12], [O^{+}14].

As expected, the massless "boost-invariant" p_{T} scheme and the p_{T} scheme result (see fig. 4.3, right) in exactly the same jet spectrum, since the manual and the FastJet-included preprocessings are equivalent. Surprisingly, the p_{T} scheme with FastJet's preprocessing needs overall a roughly 10% longer calculation time than the scheme with manual rescaling. As a consequence, the recommended choice is the "boost-invariant" p_{T} scheme with the user-programmed processing of $E = p$. In general the choice of the recombination scheme seems to have a negligible effect compared to the influence of the variety of other PYTHIA and FastJet settings.

4.2.3 Background Subtraction Methods

In contrast to Pb+Pb collisions, p+p collisions contain significantly lower momentum densities from background processes. Nevertheless also in p+p collisions the contributions from multiple parton–parton interactions, radiation effects and beam remnants can be analysed (e.g. in [A+11b]) and subtracted in order to improve the jet reconstruction in its sense of representing the hard initial scattering and with the aim to ensure comparability between different collision systems. Mainly two methods for the subtraction of underlying-event contributions from clustered jet spectra are used, and will be compared in this section with respect to their influence on PYTHIA jet spectra. In the constant approach, a homogeneous background density ρ is determined and subtracted from every jet. Naturally this approach requires the knowledge of the jet area A_{Jet}, which can be determined, e.g. in the FastJet algorithms (see sec. 3.3.2). The corrected jet momentum is defined as

$$p_{\mathrm{T,sub}} = p_{\mathrm{T}} - \rho \cdot A_{\mathrm{Jet}}. \tag{4.2}$$

The values used in this work for ρ at centre-of-mass energies 2.76 TeV are 2.1 GeV per unit area for full jets and 1.5 GeV per unit area for charged jets, respectively. This density has been determined in [A+13b] in di-jet analyses, supplemented by PYTHIA 6 calculations, by evaluating regions perpendicular to the leading jet and its backward direction. The region is oriented transverse to the hard scattering and thus assumed to be set by the underlying-event.

The second approach acts with the same idea, but on an event-by-event base. For each collision event, the complete momentum within two cones with the radius R (same parameter as set in the jet finder) is summed. Both cones are back-to-back to each other and perpendicular to the leading jet of the event. The average momentum density within these two cones is again considered to describe the momentum density of the background in this event.

Fig. 4.5 shows the ratio of charged jet spectra generated with the constant subtraction as well as with the perpendicular cone method, each divided by the uncorrected jet spectrum. The jet reconstruction was done with the anti-k_{T} algorithm and $R = 0.4$. Statistical flucutations from PYTHIA are fully excluded, since all spectra have been clustered from the same collision events. PYTHIA was set to 2.76 TeV proton–proton collisions. Both methods are compatible above a jet p_{T} of 60 GeV. For smaller p_{T} the constant approach results in lower estimations of the corrected jet cross section. In consequence, the same correction technique should be chosen for the comparison of different jet spectra. The same ratios from jet reconstruction with $R = 0.2$ in fig. 4.4 show similar characteristics as before with $R = 0.4$, while the effect is in general weaker. The different corrections are compatible for $p_{\mathrm{T}} > 40$ GeV. Furthermore it should be noted that general arguments against an "underlying-event correction" exist, since also the underlying effects are just a physical part of the proton–proton collision. Nevertheless the correction methods of different jet reconstructions should necessarily be matched.

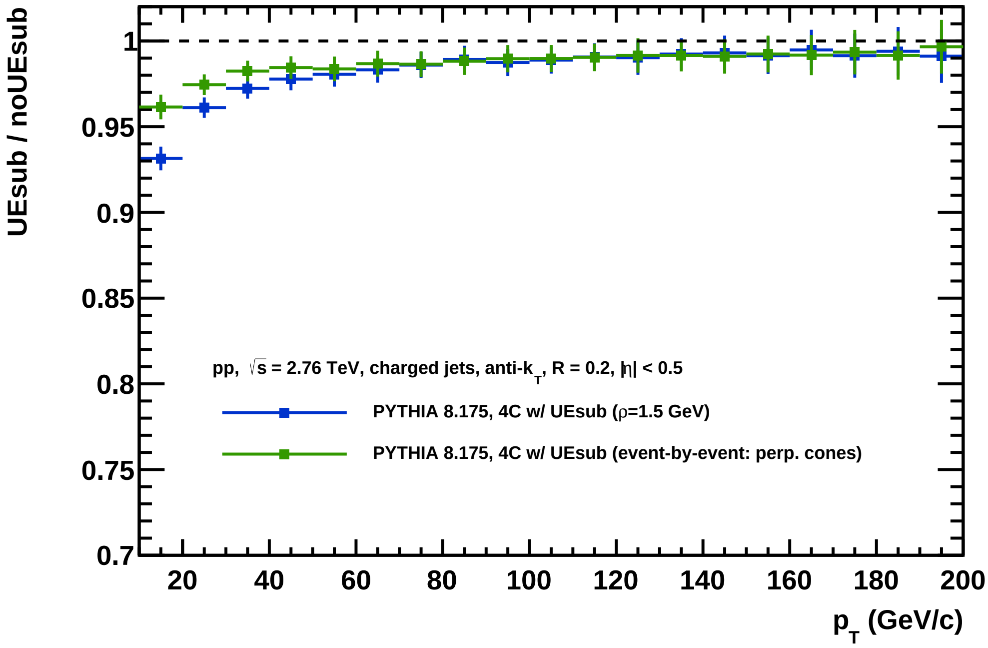

Figure 4.4: Ratio of charged jet spectra at 2.76 TeV with two different subtraction approaches of the underlying-event, divided by an uncorrected jet spectrum, anti-k_T jet reconstruction with $R = 0.2$.

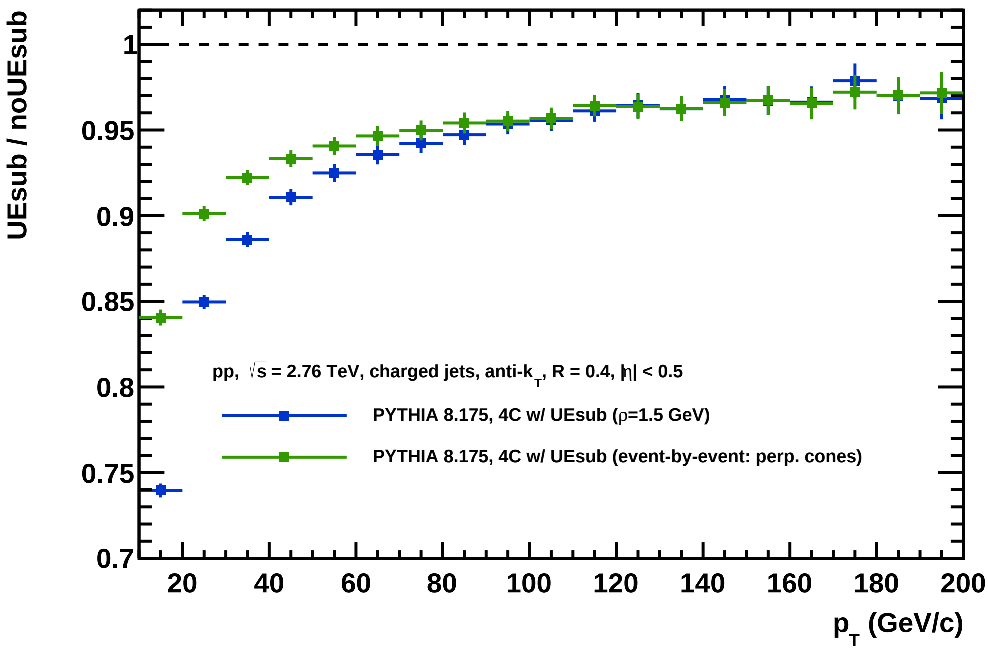

Figure 4.5: Ratio of charged jet spectra at 2.76 TeV with two different subtraction approaches of the underlying-event, divided by an uncorrected jet spectrum, anti-k_T jet reconstruction with $R = 0.4$.

4.2.4 Jet Area Distribution and Cuts

In order to exclude combinatorial jets generated by multiple incoherent processes which are not directly associated with one hard process, some jet reconstructions of measured data reject jets with an area smaller than $0.6\pi R^2$ [Haa15b], wherein R is the resolution parameter of the clustering algorithm. The following analysis checks wether this cut is relevant in p+p jet spectra as computed in this work. The presented jet areas from PYTHIA calculations have been determined with the "active area with explicit ghosts" method (see sec. 3.3.2) from the FastJet algorithm. The ghost area is chosen to 0.01 with a mean ghost momentum of $p_T = 10^{-100}$ GeV. The area distributions for charged jets from 5.02 and 7.00 TeV p+p collisions are shown for anti-k_T reconstructions with $R = 0.2$ in fig. 4.6 and with $R = 0.4$ in fig. 4.7, including all jets with p_T from 20 to 120 GeV. The cut value $0.6\pi R^2$ is marked with a black dashed line, the expected area πR^2 with a green dashed line. All area distributions have been fitted in a first guess with Gaussian functions, results are provided in tab. 4.1.

Table 4.1: Parameters of Gaussian fits to the jet area distributions from fig. 4.6 and 4.7.

R	$\sqrt{s}$	$0.6\pi R^2$	πR^2	μ	σ
0.2	5.02	0.0754	0.1257	0.1236 ± 0.0001	0.01522 ± 0.00003
0.2	7.00	0.0754	0.1257	0.1237 ± 0.0001	0.01536 ± 0.00003
0.4	5.02	0.3016	0.5027	0.5021 ± 0.0001	0.02198 ± 0.00005
0.4	7.00	0.3016	0.5027	0.5023 ± 0.0001	0.02230 ± 0.00005

The area cut threshold is for all shown combinations located outside the 3σ environment of the corresponding area distribution, as far as only these Gaussian fits are taken into account. Improved fitting results for the regions around the expected area πR^2 should be possible with Poissonian fitting, since the area is, owing to the FastJet procedure, determined as $N \cdot ghostarea$. The more important deviations are visible outside the mid-regions: the real distribution for $R = 0.4$ shows conspicuous structures left and right from the fitting. In this context, it is important to note that also in the real distributions less than 0.1% of the jets are affected by the cut in the shown or in arbitrary parts of the shown p_T range. In consequence the influence of an area cut with the proposed threshold on the jet spectra from PYTHIA calculations can be neglected. The same scenario with full jets leads to an equivalent result.

The shape of the area distribution from reconstruction with $R = 0.4$ in fig. 4.7 is highly similar to a δp_T distribution of jets in [A$^+$12a], resulting after the embedding of additional jets into a given event. The left-hand-side structures are interpreted there as a consequence of jet splitting into (at least) two smaller jets, the right-hand-side tail is associated with jet merging. The description of splitting/merging seems to be equivalent in both variables δp_T and jet *area*, while the splitting/merging is visible in the area distribution without triggering these effects via embedding processes. Parallel to the area distribution from the lower jet resolution parameter in fig. 4.6, also the δp_T result for $R = 0.2$ in [A$^+$12a] does not show the explicit splitting/merging effects, which are visible for $R = 0.4$.

Comparable structures as in fig. 4.6 and 4.7 are visible in the jet area distributions of 7 TeV p+p data measured with the ALICE experiment [Haa15a].

All distributions are stable against changes of the p_T range, as can be seen in fig. 4.8. Thus, an area cut does not take influence on jet spectra, regardless of the examined p_T window. The additional structures on both sides of the main peak slightly decrease with the stronger collimation of jets at higher p_T, which is consistent with the splitting/merging interpretation.

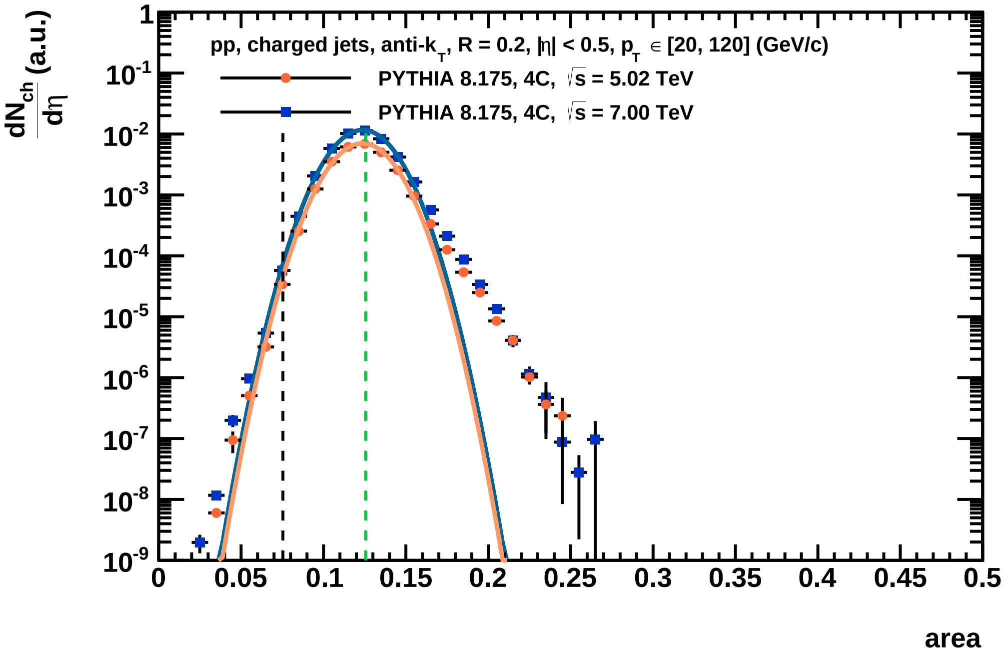

Figure 4.6: Area distributions of charged jets from 5.02 and 7.00 TeV pp calculations in PYTHIA. The jets are reconstructed with $R = 0.2$ in anti-k_T, the areas have been determined with "active areas, explicit ghosts" in FastJet. The dashed black line is placed at $0.6\pi R^2$, the jet area cut. The dashed green line marks πR^2.

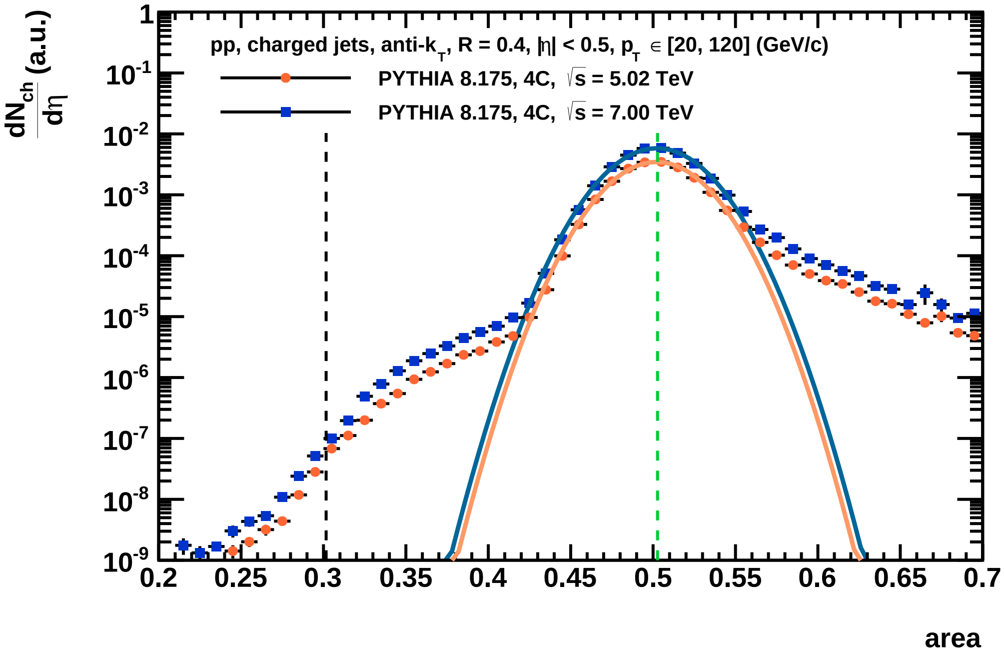

Figure 4.7: Area distributions of charged jets as in fig 4.6, reconstructed with $R = 0.4$.

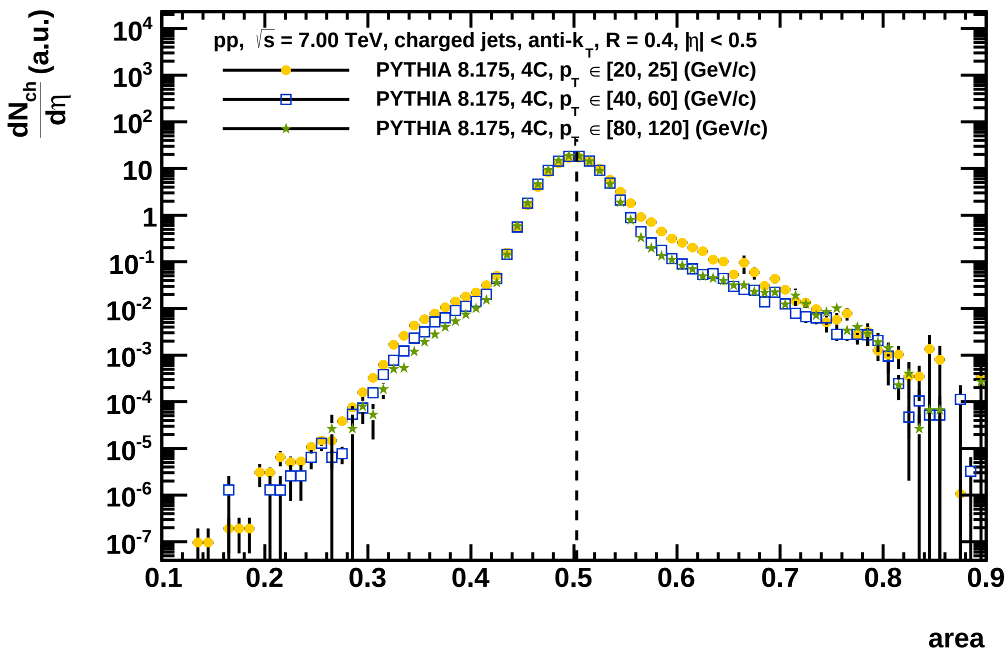

Figure 4.8: Normalised area distributions of charged jets from 7.00 TeV pp calculations in PYTHIA for different p_T ranges. Jets are reconstructed with $R = 0.4$ in anti-k_T, the areas have been determined with ”active areas, explicit ghosts“ in FastJet. The dashed black line is placed at πR^2.

4.2.5 PYTHIA Tunes

Calculations in PYTHIA consist of subprocesses for the hard collision, fragmentation, showering and multiple parton interactions. The results of these subprocesses depend on a variety of parameters, whose best settings can be obtained from tuning the overall prediction with respect to measured data. Such collections of calibrated settings are available in PYTHIA as “tunes”. The original values of PYTHIA 8, available with the configuration `tune=1`, have been determined from comparison with data from LEP1, which was an electron–positron collider experiment at CERN [SCD+15]. Tune 1 (setting `tune=2`) introduced first changes by data comparison concerning initial-state radiation and multiple parton interactions from Peter Skands in 2009. Tunes 2C (`tune=3`) and 2M (`tune=4`) from comparisons to measurements at the Tevatron experiment are based on the CTEQ 6L1 (2C) and MRST LO** (2M) parton distribution functions, respectively and have been published in 2010 [SC10]. Comparisons with LHC data led to tune 4C (`tune=5`) in the end of 2010, based on 2C. Tune 4C is the default tune of PYTHIA 8.175 as used in this analysis.

The values of the single tunes are listed in tab. 4.2. Newer PYTHIA versions since 8.200 prefer the newly invented “Monash 2013” tune, which uses the NNPDF2.3 parton distribution functions and $\alpha_S = 0.130$, tuned to results from the ATLAS experiment at CERN and further studies of the underlying-event [SCD+15].

In addition to these presets, two custom tunes based on the preset 4C have been used to reach a better agreement of calculations and measured spectra. These tunes will be called t205 for the configuration `SigmaProcess:Kfactor=0.7` and t505 for `SigmaProcess:alphaSvalue=0.1265` in the following. The K-factor is multiplied to all cross sections of the hard collision process except multiple parton interactions. `SigmaProcess:alphaSvalue` sets the α_S value in the hard process.

Table 4.2: Specific values of the predefined tunes in PYTHIA 8.1 for particle generation and other subprocesses according to the PYTHIA 8.175 source code and [SC10]. Non-listed parameters are set to the original values of PYTHIA 8.

Parameter	(original values) `tune=1`	Tune 1 `tune=2`	Tune 2C `tune=3`	Tune 2M `tune=4`	Tune 4C `tune=5`
SigmaProcess:alphaSvalue	0.1265	0.1265	0.135	0.1265	0.135
SpaceShower:rapidityOrder	off	off	on	on	on
SpaceShower:alphaSvalue	0.127	0.137	0.137	0.130	0.137
SpaceShower:pT0ref	2.2	2.0	2.0	2.0	2.0
MultipleInteractions:alphaSvalue	0.127	0.127	0.135	0.127	0.135
MultipleInteractions:pT0ref	2.15	2.25	2.320	2.455	2.085
MultipleInteractions:ecmPow	0.16	0.24	0.21	0.26	0.19
MultipleInteractions:bProfile	2	1	3	3	3
MultipleInteractions:expPow	0.4	0.4	1.60	1.15	2.0
BeamRemnants:reconnectRange	2.5	10.0	3.0	3.0	1.5
SigmaDiffractive:dampen	off	off	off	off	on
SigmaDiffractive:maxXB	n/a	n/a	n/a	n/a	65
SigmaDiffractive:maxAX	n/a	n/a	n/a	n/a	65
SigmaDiffractive:maxXX	n/a	n/a	n/a	n/a	65

The further parameters of the preset tunes are, according to [SC10]:

- The settings `alphaSvalue` result in a change of the coupling α_S in the corresponding subprocess.
- `SpaceShower:rapidityOrder=on` vetoes rapidity-unordered emissions of initial-state radiation, helps to dampen the underlying-event to measured values.
- The `pT0ref` parameters set a regularisation of the initial-state showering and the multiple parton interaction framework. These settings affect particles at smaller p_T, the charged multiplicity and the underlying-event.
- `MultipleInteractions:ecmPow`, `-bProfile` and `-expPow` change the regularisation and matter profiles in the multiple parton interaction framework.
- `BeamRemnants:reconnectRange` sets the probability of colour reconnection with harder systems.
- The `SigmaDiffractive` parameters allow to set and tune diffractive cross sections [SCD+15].

Fig. 4.9 and 4.10 show the ratio of anti-k_T jet spectra from the various PYTHIA preset and custom tunes divided by the same spectrum from the default tune 4C. PYTHIA has been set to p+p collisions at 5.02 and 7.00 TeV, the jet resolution parameter R was 0.4. A comparison to measured data is shown in sec. 4.4.

The ratios do not show major differences between 5.02 and 7.00 TeV. The energy scaling behaviour of the tunes will be analysed in detail in the following section. As expected from the similar values, the original PYTHIA configuration and tune 1 result in a very similar shape. Both yield, presumably due to the smaller α_S value, an overall smaller jet cross section. Tune 2C shows nearly no difference to 4C on the available level of statistics. Tune 2M with its different PDFs MRST LO** results, even if set to a smaller α_S, in a cross section that is up to 30% higher. This maximum of the shaped ratio is located in a broad mid-p_T range.

The custom tune t205 with a K-factor of 0.7 results in a jet spectrum which is fully compatible with that from its original tune 4C, scaled with the same factor of 0.7 after the jet clustering. The p-value between both histrograms is 1. As a consequence, a general scaling of the initial hard cross sections can be replaced by the same scaling applied to the resulting jet spectrum.

Custom tune t505 shows the effects of a change of α_S in the hard process. The 6.3% smaller coupling entails a decrease of about 15% at a p_T of 20 GeV, reducing to a decrease of about 10% at 200 GeV.

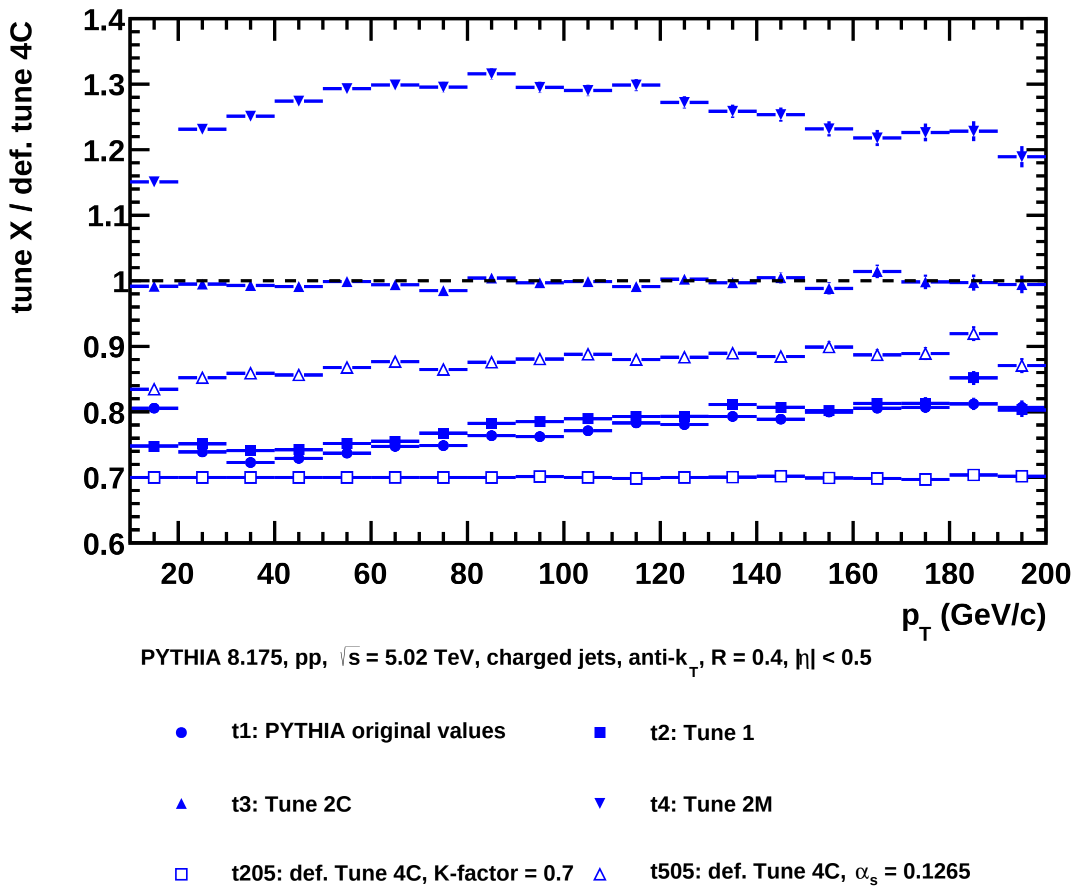

Figure 4.9: Ratio of charged jet spectra reconstructed from different PYTHIA tunes to the jet spectrum with PYTHIA's default tune 4c for a collision energy of 5.02 TeV. The numbering 'tX' follows the internal PYTHIA names, t205 and t505 are custom tunes discussed in the text of this section.

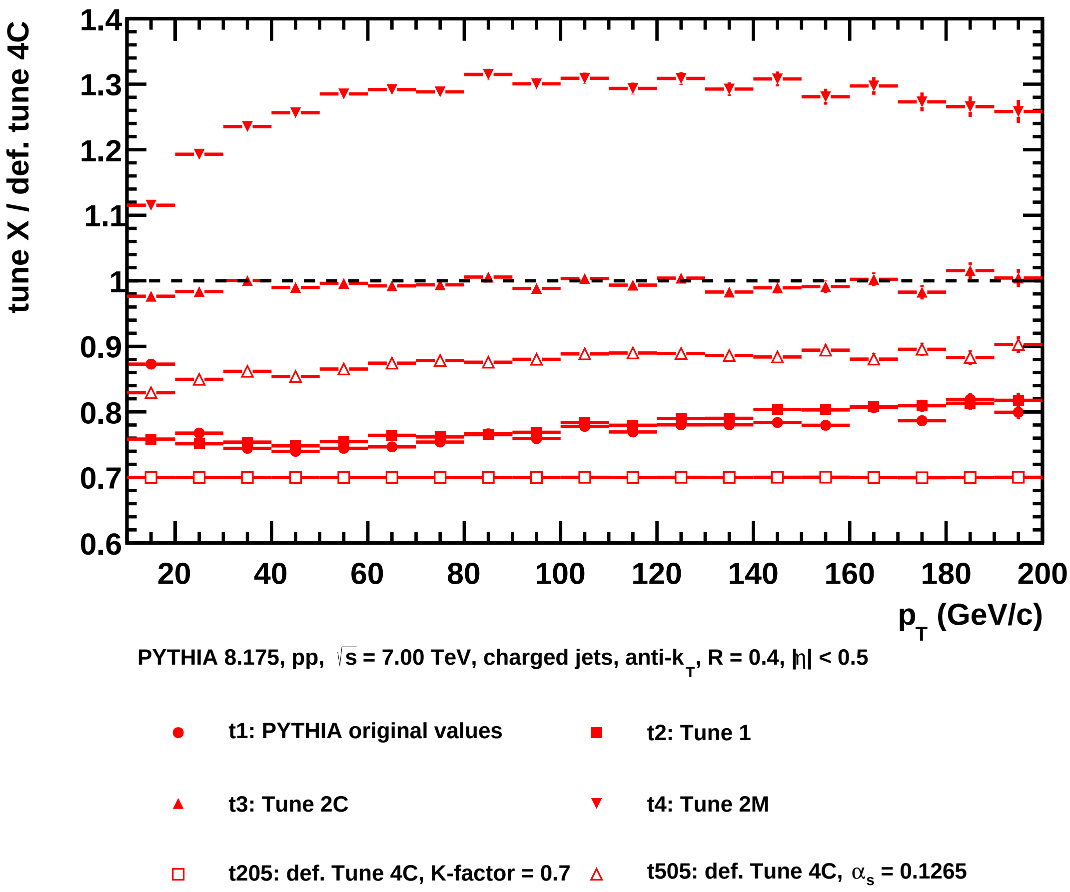

Figure 4.10: Ratio of charged jet spectra reconstructed from different PYTHIA tunes to the jet spectrum with PYTHIA's default tune 4c for a collision energy of 7.00 TeV. The numbering 'tX' follows the internal PYTHIA names, t205 and t505 are custom tunes discussed in the text.

4.3 Energy Scaling in PYTHIA

The p_T-dependent scaling function between the jet spectra from 7.00 TeV and 5.02 TeV p+p collisions is necessary for the construction of a 5.02 TeV (reference) jet spectrum from spectra of 7 TeV p+p collisions. A p+p reference at this energy is needed for the comparison with p+Pb collisions at $\sqrt{s_{NN}} = 5.02$ TeV. Up to today no direct measurements from p+p collisions at 5.02 TeV are available.

It is not possible to predict in a trivial way the influence of the variety of tunable settings for the hard collision process, for showering and hadronisation and further initial- and final-state effects in PYTHIA on the jet energy scaling. Fig. 4.11 shows the resulting scaling function for the preset and two custom tunes as listed in tab. 4.2. During the analysis a clear trend to a smaller band for higher statistics was visible, while the question of full convergence cannot be decided within the available statistical level.

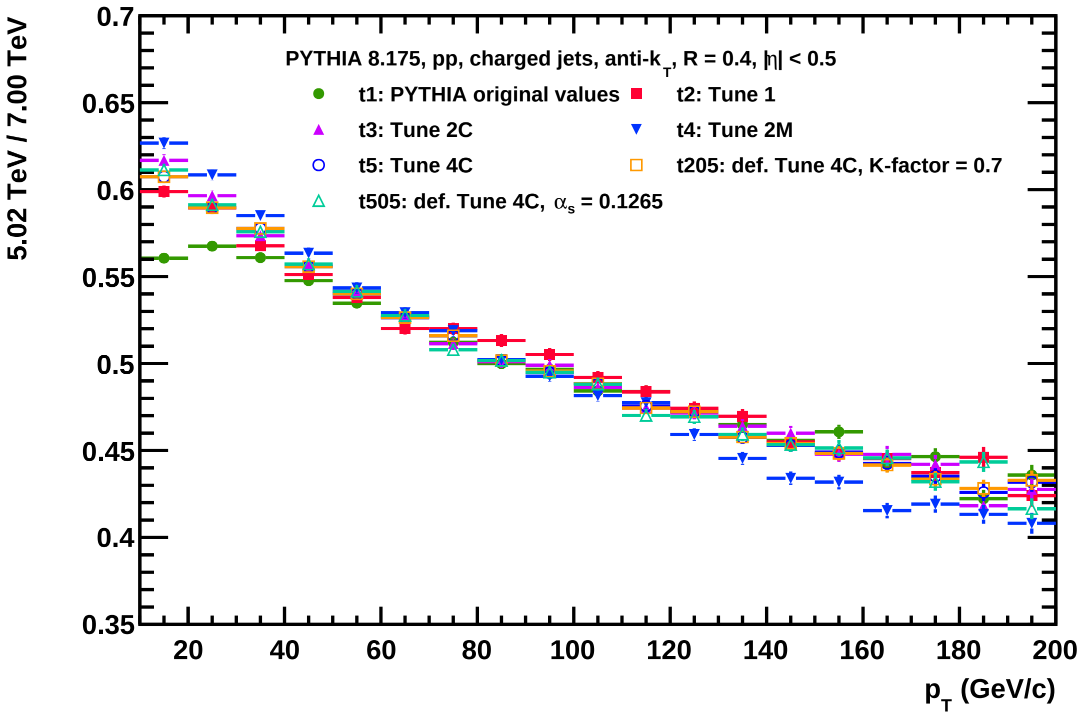

Figure 4.11: Energy scaling for charged jets with $R = 0.4$, reconstructed from different PYTHIA tunes as in fig. 4.9 and 4.10 before. Tab. 4.3 and 4.4 show statistical compatibility checks between the different tunes and tune 4C.

Tab. 4.3 and 4.4 list the χ^2/NDF and p-values for each analysed tune to PYTHIA 8.175's default tune 4C in the region from 20 to 140 GeV and in the region between 40 and 140 GeV, respectively. The agreement is in general better for tunes using the same parton distribution functions as tune 4C: CTEQ 6L1. For p_T in 40 to 140 GeV, the jet energy scaling of all checked tunes is compatible in the sense of a requested p-value of at least 5%. The same check for p_T between 20 and 140 GeV allows to state this compatibility only for tune 2C and the two custom variations of 4C (K-factor=0.7 or $\alpha_S = 0.1265$) to the preset 4C.

Table 4.3: Statistical compatibility between the jet energy scaling functions from different PYTHIA tunes and tune 4C for p_T between 20 and 140 GeV.

Tune X to Tune 4C	χ^2/NDF	p-value
(original values, t1)	4.03	0.00002
1	2.36	0.0087
2C	0.59	0.82
2M	3.23	0.0004
4C with K-factor = 0.7	0.01	1.00
4C with $\alpha_S = 0.1265$	0.48	0.90

Table 4.4: Statistical compatibility between the jet energy scaling functions from different PYTHIA tunes and tune 4C for p_T between 40 and 140 GeV.

Tune X to Tune 4C	χ^2/NDF	p-value
(original values, t1)	1.18	0.31
1	1.89	0.06
2C	0.28	0.97
2M	1.84	0.06
4C with K-factor = 0.7	0.01	1.00
4C with $\alpha_S = 0.1265$	0.55	0.82

From the comparison of the two ranges it is obvious that most of the differences in the energy scaling are located in the jet p_T region from 20 to 40 GeV. Also above 140 GeV the scaling behaviour seems to differ, while the result in the mid-p_T region is comparable for all tunes.

The compatibility between the resulting energy scaling functions can furthermore be estimated with the double ratio from fig. 4.12. The energy scaling of the different tunes has been divided by the same energy scaling function as in tune 4C. In agreement with the statistical check before, tune 2C and K-factor variation of 4C are compatible with the null hypothesis (unity) for p_T between 20 and 140 GeV, while the α_S variation causes the jet energy scaling to deviate.

A decision for one of the partially different energy scaling functions cannot be made without further checks on measured data. Nevertheless the scaling functions of the newer tunes 2C and 4C are self-consistent over a broad p_T range and should be preferred against older tunes due to the better agreement of their calculated spectra to measured data, as shown in the following sections.

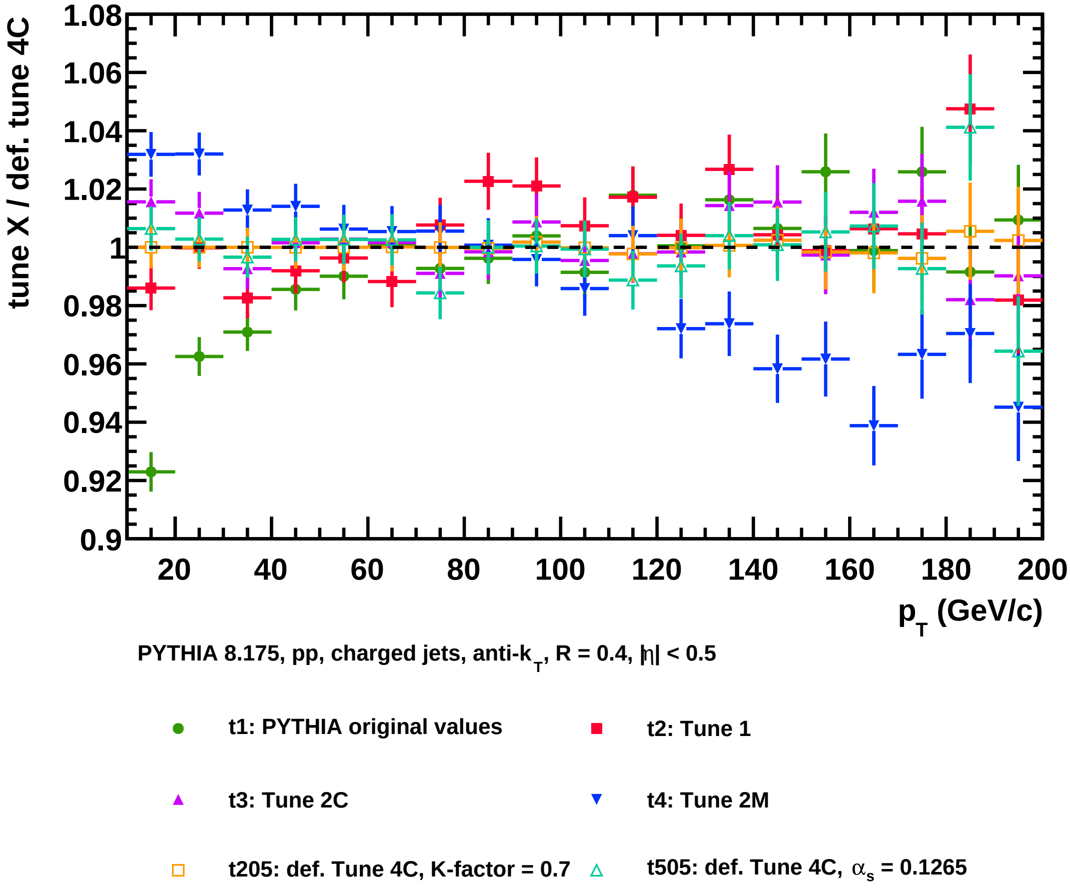

Figure 4.12: Energy scaling (5.02 over 7.00 TeV) for charged jets from different PYTHIA tunes, clustered with $R = 0.4$, divided by the same jet energy scaling of PYTHIA's default tune 4C.

4.4 Comparing PYTHIA Calculations to Measured ALICE Data

4.4.1 PYTHIA to ALICE Data at 2.76 TeV

The results from PYTHIA have been checked in comparison to published ALICE measurements, both for the p_T spectrum of generated particles and the jet spectrum after anti-k_T reconstruction. Fig. 4.13 shows the ratio of PYTHIA/ALICE for charged particles within $|\eta| < 0.8$ for p_T between 8 and 32 GeV as published in [A+13a]. Compared to this measurement, PYTHIA overestimates the spectrum by about 15 to 20%. For p_T between 8 and 14 GeV a decrease of the ratio is visible. An explanation of this shape can possibly be found in the way in which PYTHIA takes some NLO effects into account, with corrections which are located primarily in the soft region. For p_T above 15 GeV the ratio is compatible with a constant. The uncertainties for the PYTHIA calculation are from statistical fluctuations only, while the uncertainties of the ALICE data are the combination of both the statistical and the systematic contribution.

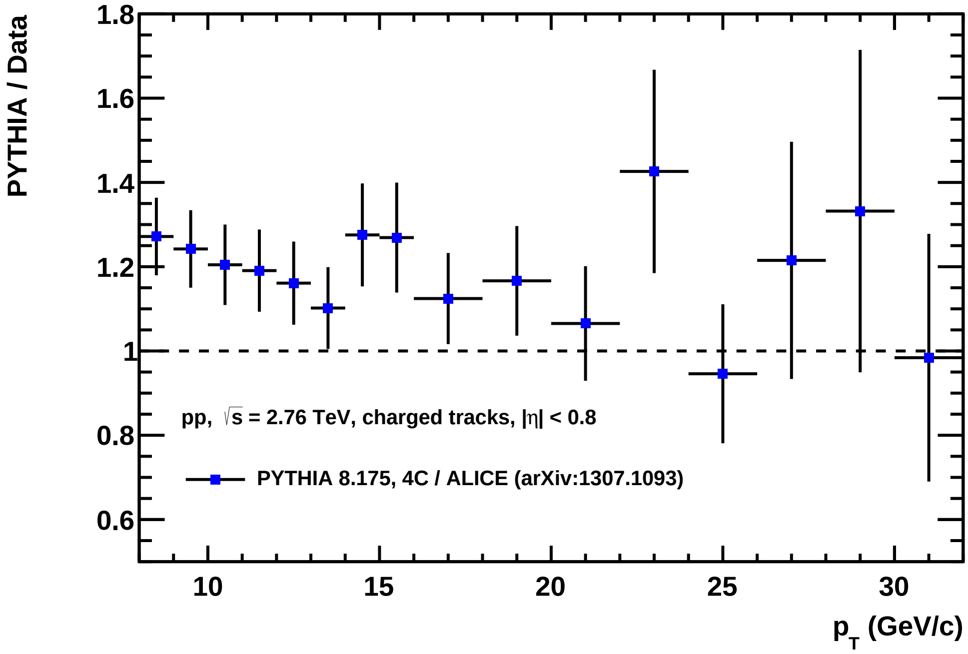

Figure 4.13: Ratio of charged tracks at 2.76 TeV from PYTHIA and ALICE. PYTHIA over reference data as published in [A+13a]. Statistical and systematic uncertainties of the ALICE data have been combined.

Fig. 4.14 shows a comparison with jet reconstructions ($R = 0.2$ and 0.4) from ALICE data, run 2011c2, for p_{T} between 20 and 100 GeV. The jet spectra were provided by Michal Vajzer (Czech Technical University in Prague, Czech Republic) during a stay in the local working group for common studies [Vaj13]. The momentum of each jet in the reconstruction from PYTHIA's calculation has been corrected for the underlying-event in dependence of the jet area A_{Jet} and with a constant background density to $p_{T,sub} = p_{\mathrm{T}} - A_{Jet} \cdot 1.5$ GeV (see sec. 4.2.3), in the same way as chosen in the ALICE reconstruction. For both jet resolution parameters, the ratio shows a falling trend over the full p_{T} range, while the result is compatible with a constant within its statistical uncertainties. Moreover the ratio for $R = 0.4$ coincides with unity over the full transverse momentum range.

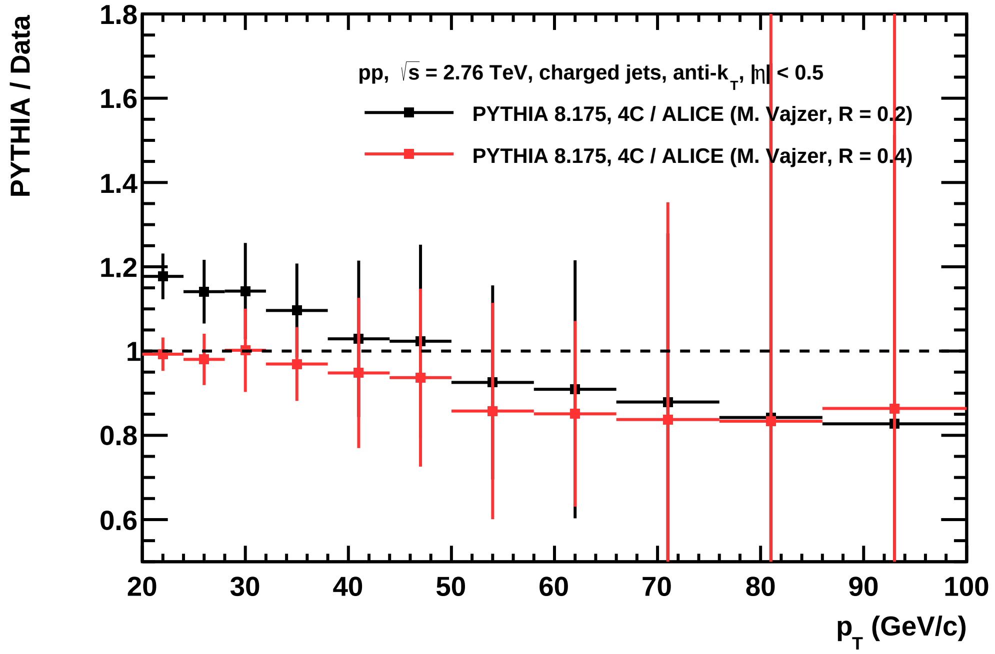

Figure 4.14: Comparison of charged jets at 2.76 TeV reconstructed with $R = 0.2$ and 0.4. Reference data from unfolding tasks of Michal Vajzer [Vaj13].

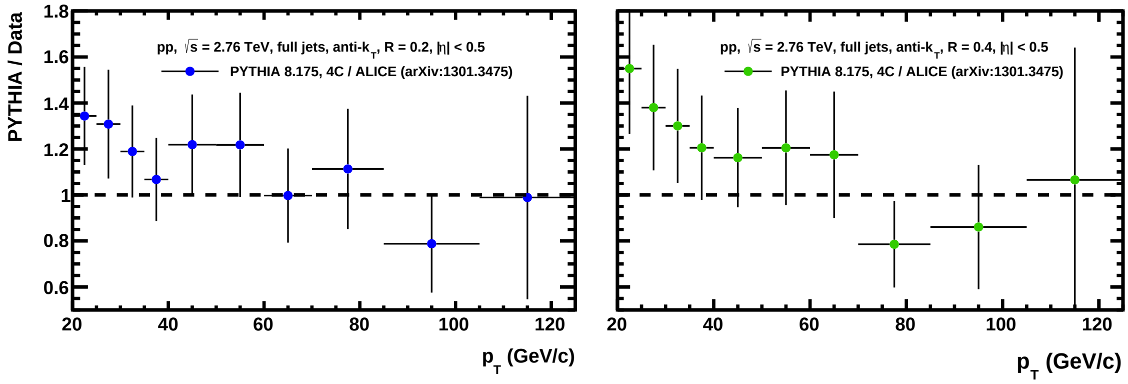

Figure 4.15: Comparison of full jet spectra at 2.76 TeV from PYTHIA and ALICE. The ALICE spectrum is published in [A+13b]. Reconstructed with $R = 0.2$ (left) and $R = 0.4$ (right). The uncertainties of the measured data are combined from the statistical and systematic parts.

A similar result was obtained from the comparison of full jets from ALICE measurements for p_{T} within 20 to 125 GeV, which have been published in [A+13b]. Here, the underlying-event has been corrected for a constant background density with $p_{T,sub} = p_{\mathrm{T}} - A_{Jet} \cdot 2.1$ GeV both for PYTHIA and ALICE. The falling trend of the ratio PYTHIA/ALICE, as seen in the comparison before, was reproduced for $R = 0.2$ and $R = 0.4$ in fig. 4.15. PYTHIA overestimates the spectrum in the lower half of the analysed p_{T} range.

Fig. 4.16 shows the jet structure ratio

$$\mathcal{R}(0.2, 0.4) = \frac{\mathrm{d}^2\sigma(R = 0.2)/\mathrm{d}p_\mathrm{T}\mathrm{d}\eta}{\mathrm{d}^2\sigma(R = 0.4)/\mathrm{d}p_\mathrm{T}\mathrm{d}\eta} \tag{4.3}$$

for the charged jet spectra from ALICE ([A$^+$13b]) and PYTHIA. $\mathcal{R}$ is a measure of the angular distribution of particles in the jet and in this sense a description of the collimation of jets around their main axis. The calculation of $\mathcal{R}$ does not include a check for the geometrical coincidence of the jets at different R, but is a general measure on the level of p_T spectra. A high value of $\mathcal{R}$ close to unity implies a highly collimated transverse momentum in the jets. Hence the typical increase of $\mathcal{R}$ for higher p_T indicates the stronger collimation of these more energetic jets. PYTHIA agrees with the ALICE reconstruction within the statistical uncertainties. A comparison of both functions results in $\chi^2/NDF = 1.03$. Slight deviations can be explained with systematic differences between the reconstructions at different R, while a full addition of the systematic uncertainties in counter and denominator is obviously prohibited by the correlations of both reconstructions.

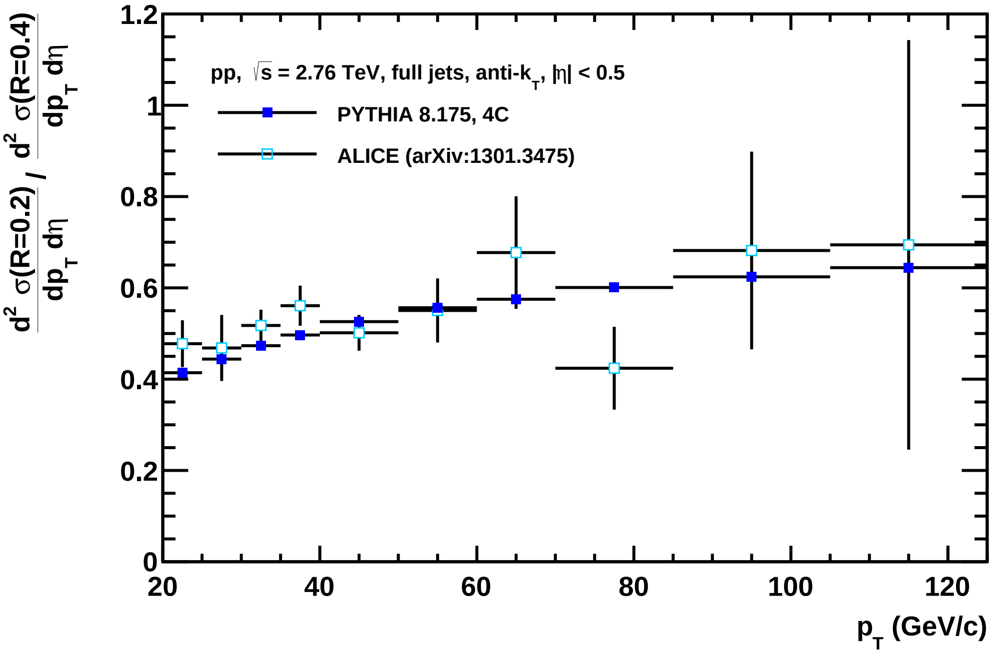

Figure 4.16: The jet structure ratios $\mathcal{R}(0.2, 0.4)$ of full jet cross sections from pp collisions at 2.76 TeV from PYTHIA and [A$^+$13b]. The last data point is not shown in the ALICE publication.

4.4.2 PYTHIA to ALICE Data at 7.00 TeV

The ratio of a charged particle spectrum at 7 TeV for $|\eta| < 0.8$ from PYTHIA's tune 4C to the ALICE charged particle spectrum as published in [A^+13a] shows a falling shape, as can be seen in fig. 4.17. PYTHIA overestimates the cross section by up to about 50% in the lower p_T region around 10 GeV. The overestimation at the collision energy of 7 TeV is more pronounced than for 2.76 TeV as shown (with a different p_T range) in fig. 4.13.

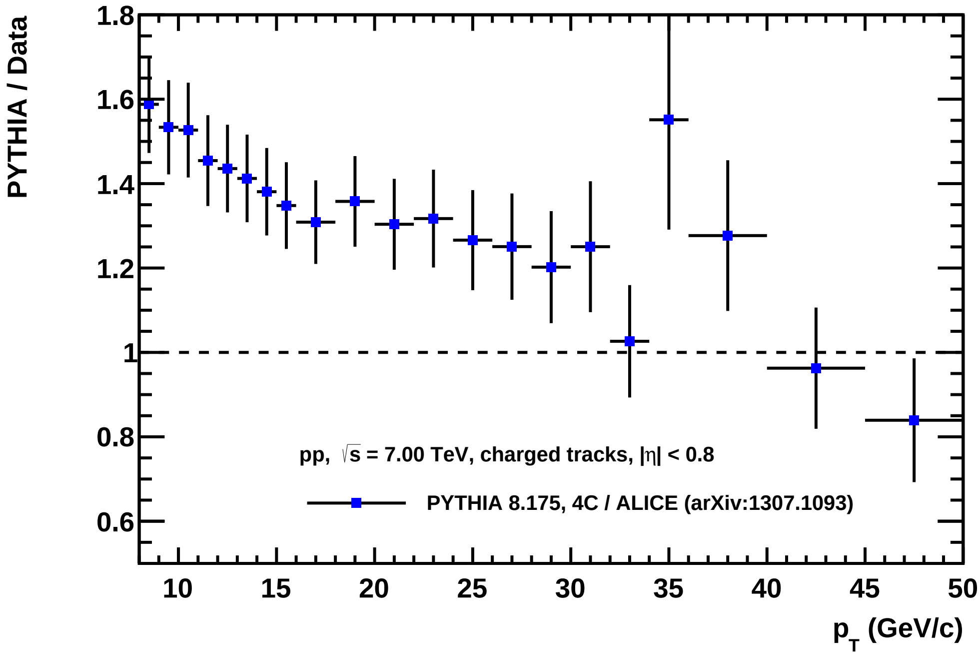

Figure 4.17: Ratio of charged particle cross sections at 7.00 TeV from PYTHIA and ALICE. PYTHIA has been configured with tune 4C. The ALICE data are published in [A^+13a]. Statistical and systematic uncertainties of the ALICE data have been combined.

The following comparisons focus on jets. Charged jet spectra from PYTHIA with all tunes 1, 2C, 2M, 4C and PYTHIA's original values (`tune=1`) as listed in tab. 4.2 and the two custom tunes t205 (4C, $K = 0.7$) and t505 (4C, $\alpha_S = 0.1265$ in the hard process) as described in sec. 4.2.5 have been compared to measured data from ALICE [A^+14a], as shown in fig. 4.18. The spectra from PYTHIA have been corrected event by event for underlying-event effects with the perpendicular cone method as described in sec. 4.2.3 in the same way as applied on the ALICE data. The best overall agreement was reached for tune t205 (4C, $K = 0.7$). For p_T between 20 and 100 GeV, a χ^2-test of t205 to the measured data achieves $\chi^2/NDF = 1.01$. PYTHIA overestimates the jet spectrum by about 10 to 20%, with a falling shape in the lower p_T region between 20 and 44 GeV.

It should be noted that with respect only to the χ^2-test, tune t505 (4C, $\alpha_S = 0.1265$ in the hard process) with $\chi^2/NDF = 0.81$ to the ALICE measurement [A^+14a] would have to be preferred against t205. In contrast, t205 is chosen in the following due to the overall better scaling. Future enhancements are possible to be reached by a combined tuning with a K-factor below one <u>and</u> a lowered α_S in the hard process of PYTHIA.

The ratio of charged jet cross sections from PYTHIA with the preferred tune t205 over ALICE data is shown in fig. 4.19 for the anti-k_T parameter $R = 0.2$ (with $|\eta_{jet}| < 0.7$) and $R = 0.4$ (with $|\eta_{jet}| < 0.5$). The ratio from $R = 0.2$ is compatible with unity, while the reconstruction with $R = 0.4$ overpredicts for $p_T < 32$ GeV.

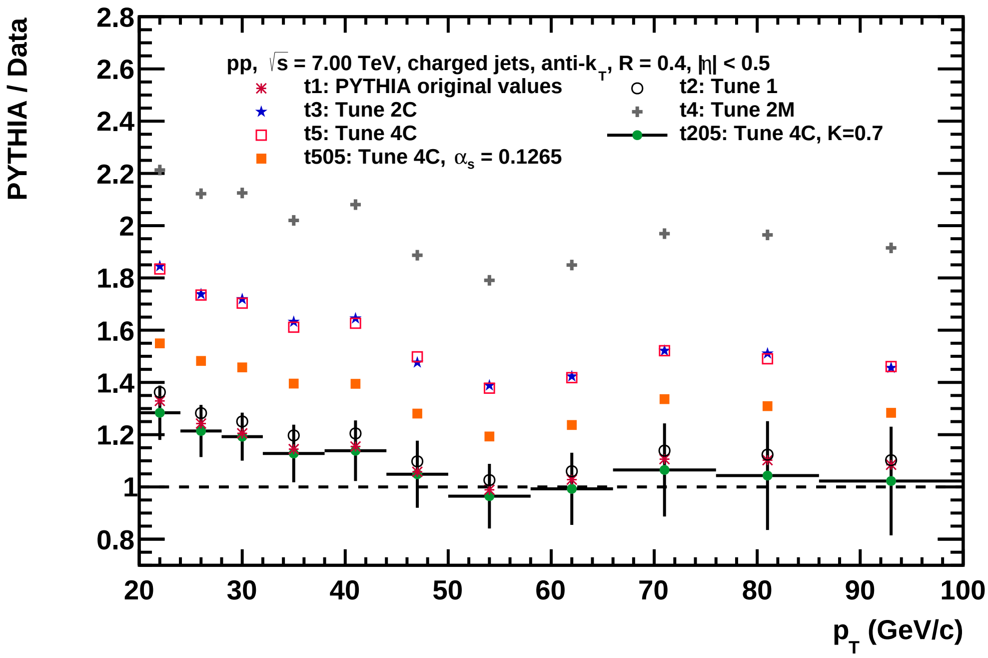

Figure 4.18: Ratio of charged jet spectra at 7.00 TeV from different tunes in PYTHIA 8.175 (see text) to ALICE data. The ALICE spectrum is published in [A+14a]. Reconstructed with $R = 0.4$. Statistical and systematic uncertainties of the ALICE data have been combined. The uncertainties of the ratios originate mainly from the ALICE measurement; thus, they are equal for all tune comparisons, while for better clarity shown only for tune t205 (4C, $K = 0.7$). The axis scaling of this plot differs from other PYTHIA/Data ratios shown in this work.

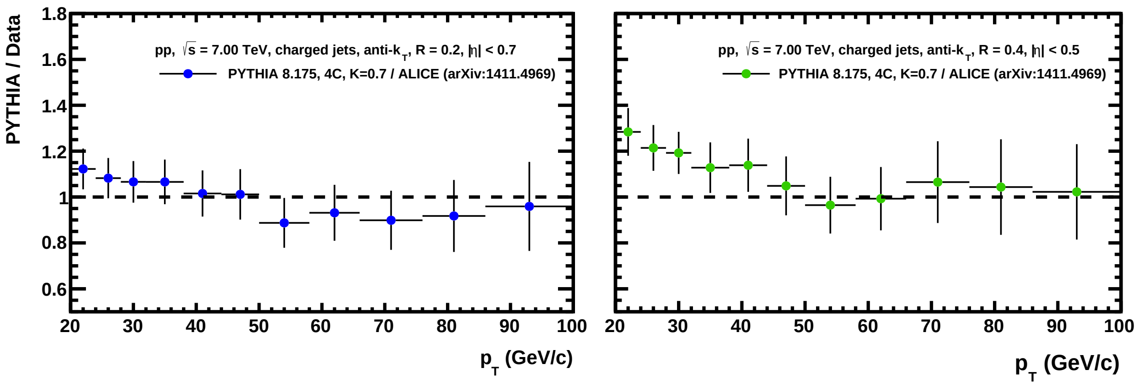

Figure 4.19: Ratio of charged jet spectra at 7.00 TeV from PYTHIA and ALICE. PYTHIA with tune 4C and a K-factor of 0.7. The ALICE spectrum is published in [A+14a]. Reconstructed with $R = 0.2$ (left) and $R = 0.4$ (right). Statistical and systematic uncertainties of the ALICE data have been combined.

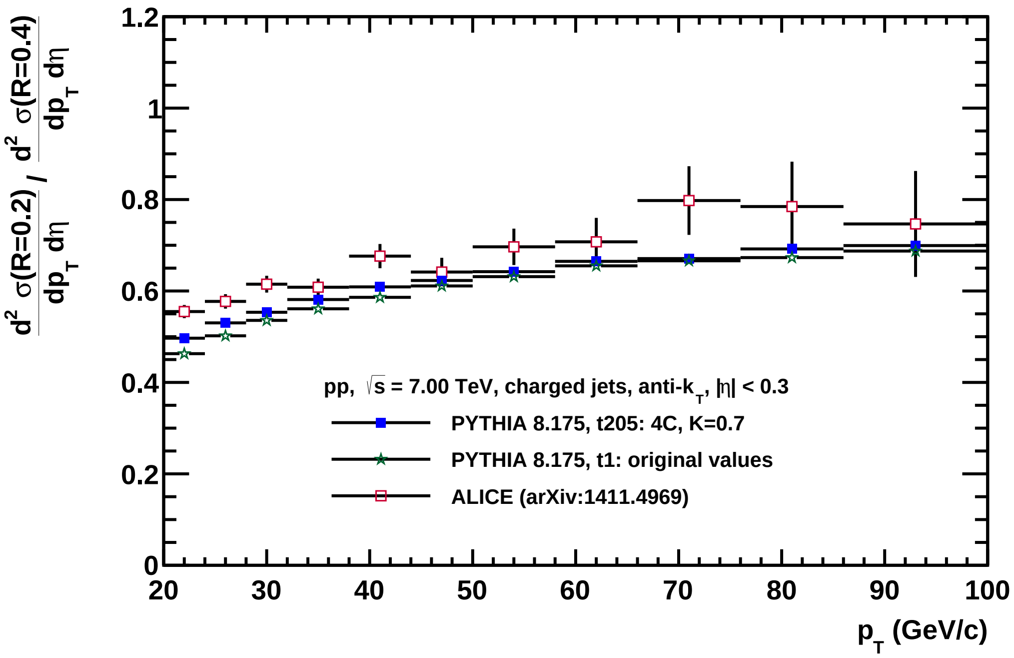

Figure 4.20: Jet structure ratios from PYTHIA (t205: tune 4C with a K-factor of 0.7 and t1: PYTHIA 8's original values) and from the ALICE charged jets as published in [A+14a].

The jet structure ratio $\mathcal{R}$ has been defined in eq. 4.3. $\mathcal{R}(0.2, 0.4)$ from PYTHIA calculations with tune 4C, $K = 0.7$ and the same ratio from ALICE [A+14a] in fig. 4.20 agree on a good level, the χ^2-test results in $\chi^2/NDF = 0.56$. Furthermore, [A+14a] depicts the jet structure ratio obtained with PYTHIA 6 calculations, tune Perugia-2011 (not shown here). Similar to the result from PYTHIA 8, $\mathcal{R}$ from PYTHIA 6 slightly underestimates the measured data, but is statistically compatible to the measurement.

A comparison of the jet structure ratio from all PYTHIA tunes and PYTHIA's original values (`tune=1`) with the structure ratio from the preferred tune t205 results in a high agreement for $\mathcal{R}$ from all tunes, except for PYTHIA's original values. $\mathcal{R}$ from none of the tunes 1, 2C, 2M, 4C and t505 deviates more than 2% from t205. In contrast, $\mathcal{R}$ from the original values deviates by up to 8% from t205 (4C, $K = 0.7$) for p_{T} between 20 and 45 GeV, as can be seen in fig. 4.20.

4.4.3 PYTHIA at 5.02 TeV

As explained before, no data from p+p collisions at 5.02 TeV have been measured up to now. The ALICE collaboration published an R_{pPb} for charged particles at this energy under the use of a 5.02 TeV reference spectrum that has been calculated from measured p+p data at 7.00 TeV with a scaling function from NLO pQCD predictions in [A+12b]. For consistency checks, the reference spectrum from the ALICE publication has been compared to a charged particle spectrum calculated with PYTHIA, tune 4C. The same comparison is shown in sec. 4.4.2 for PYTHIA to a measured charged particle spectrum at 7 TeV. The pseudorapidity is limited here both for calculation and reference to $|\eta| < 0.3$.

As shown in fig. 4.21, the PYTHIA/reference ratio is not compatible with unity and reveals an overestimation in PYTHIA by up to about 50% in the lower p_{T} region around 10 GeV. This is consistent with the observation on the charged particles at an energy of 7.00 TeV as shown in fig. 4.17. Consequently this reveals no contradiction between PYTHIA's energy scaling between 5.02 and 7.00 TeV and the NLO energy scaling as used in [A+12b].

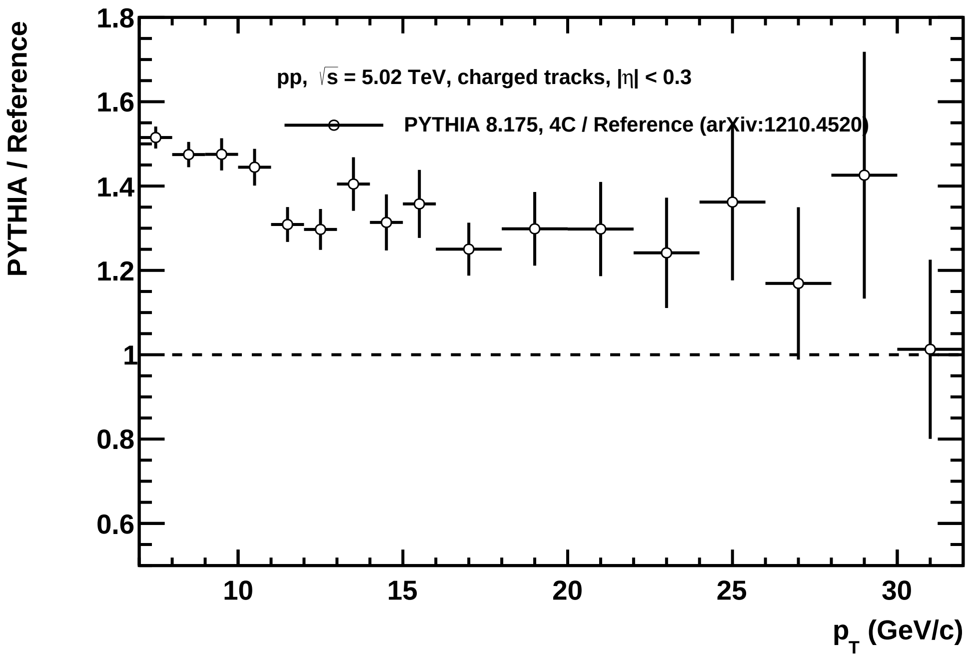

Figure 4.21: Ratio of charged particle cross sections at 5.02 TeV from PYTHIA (with tune 4C) and the reference as constructed in [A+12b] for a particle R_{pPb}.

5 POWHEG BOX as NLO Event Generator

5.1 POWHEG NLO Events in PYTHIA

To reach a higher precision in the calculation of collision events, the accuracy can be increased to the level of NLO terms in QCD processes. This chapter presents jet spectra that are based on NLO calculations of the parton scattering done by Michal Vajzer (Czech Technical University in Prague, Czech Republic) with the POWHEG BOX framework [FNO07], [ANO+10]. The used parton distribution functions of POWHEG were ID 10550 according to the LHAPDF numbering scheme, which means the use of the PDF set CTEQ6.6 with $\alpha_s(M_Z) = 0.118$ [PSH+02], [Buc14], [NLC+08]. The parameters μ for renormalisation and μ_f were both unchanged on the reference value: $\mu = \mu_f = \mu_{ref}$. Moreover, POWHEG handles divergence problems in underlying Born processes with a transverse momentum cut `bornktmin`, which was set to 1 GeV here, and with a suppression factor $k_{\mathrm{T}}^2/(k_{\mathrm{T}}^2 + \texttt{bornsuppfact}^2)$, set to $\texttt{bornsuppfact} = 40$ [ANO+11]. As described in sec. 3.2, POWHEG generates positive-weighted events under the use of NLO matrix elements and stores them in the "Les Houches Interface for User Generated Processes" format [ABB+06].

The event list for the following analysis consists of 1.6 M p+p events at $\sqrt{s} = 7.00$ TeV. The subsequent processes of showering and hadronisation have been calculated event by event with PYTHIA 8.175; to avoid double counting of NLO effects, which are partly simulated in PYTHIA, PYTHIA's PDF setting has been matched to the POWHEG setting. Systematic uncertainties of the spectrum have been tested from Michal Vajzer by variations of initial parameters to be 6% from the CTEQ PDF settings and 13% from scale variations [Vaj13].

The charged jet spectra (anti-k_{T}, $R = 0.4$) from pure PYTHIA and matched POWHEG+PYTHIA are shown in fig. 5.1. The underlying-event has been corrected with the perpendicular cone method (see sec. 4.2.3). Pure PYTHIA has been tuned to preset 4C with a K-factor of 0.7 as for the comparison with ALICE data before in fig. 4.19. The log-log plot reveals a slightly higher potential increase with p_{T} in the NLO case. The jet spectrum ratio of POWHEG+PYTHIA over PYTHIA is shown in fig. 5.2.

Obviously the NLO calculations result in smaller cross sections in the lower p_{T} region than pure PYTHIA. The comparisons of pure PYTHIA with measured data in sec. 4.4.2 revealed an overestimation in this region, which is possibly caused by PYTHIA's rough simulation of NLO effects. The comparison of the jet structure ratio $\mathcal{R}(0.2, 0.4)$ (see eq. 4.3) from the LO and NLO calculations are in good agreement, as shown in fig. 5.3.

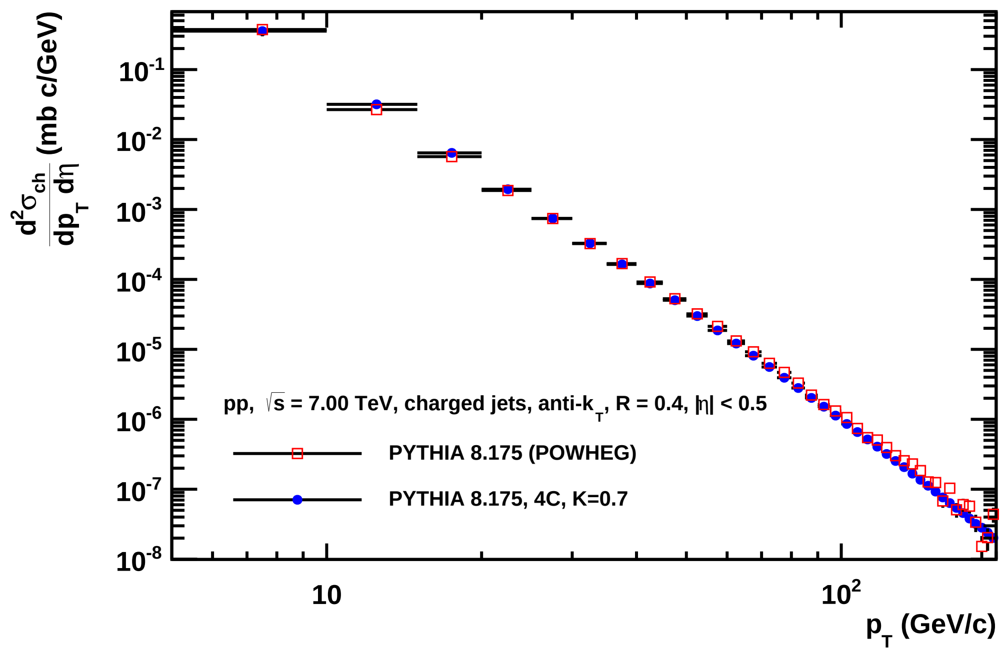

Figure 5.1: Charged jet spectra from pure PYTHIA calculations (tune 4C, K-factor = 0.7, "t205", blue symbols) and NLO calculations in POWHEG with subsequent showering and hadronisation in PYTHIA (red symbols) of pp collisions at 7.00 TeV in a log-log chart.

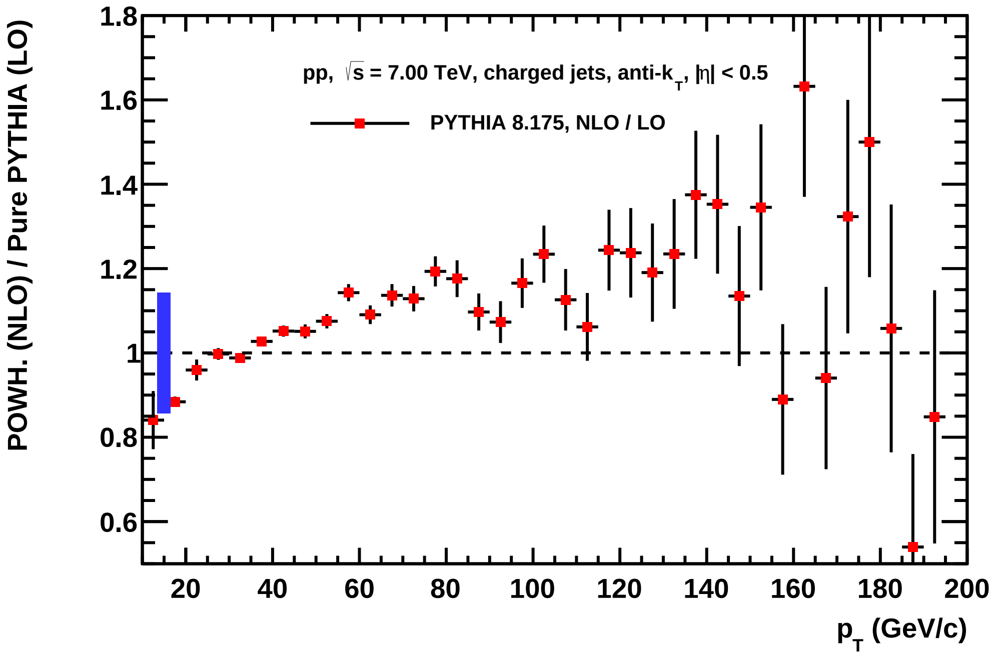

Figure 5.2: Ratio of charged jets from the POWHEG+PYTHIA generation at 7.00 TeV pp to the spectrum from a PYTHIA stand-alone generation. The blue bar marks the systematic uncertainty from settings in the POWHEG calculations.

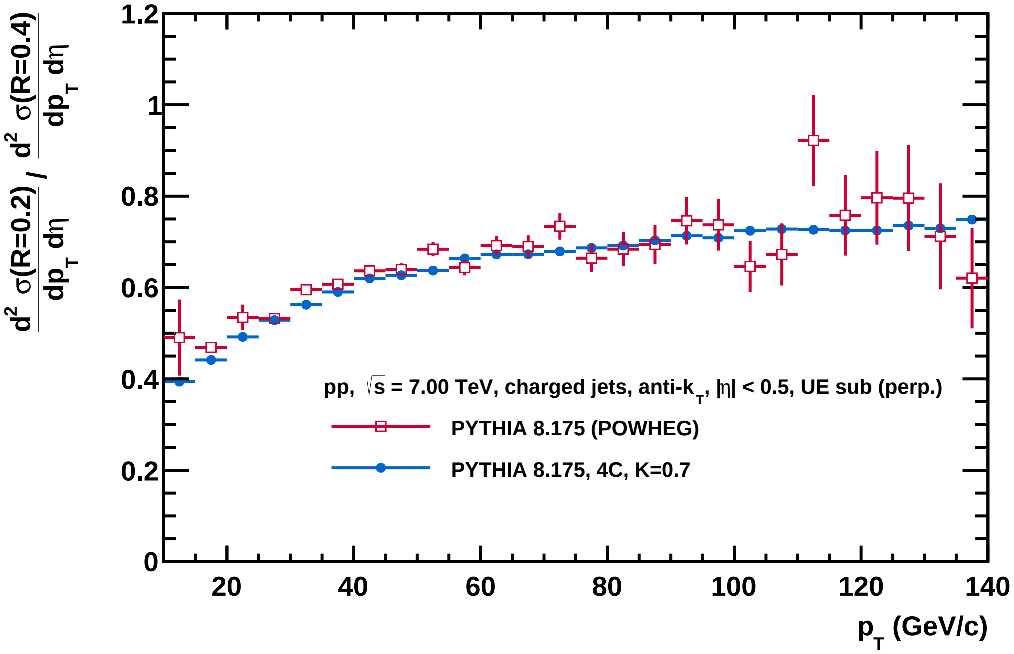

Figure 5.3: Jet structure ratios $\mathcal{R}(0.2, 0.4)$ from POWHEG+PYTHIA and PYTHIA stand-alone generations.

5.2 Comparing POWHEG to ALICE data at 7.00 TeV

Fig. 5.4 shows the ratio of charged jet spectra from POWHEG+PYTHIA 8.175 over measured ALICE data from [A+14a]. Both jet spectra are corrected for underlying-event contributions with the perpendicular cone method (sec. 4.2.3). The same comparison is shown in fig. 4.19 for calculations in LO with pure PYTHIA. The chosen settings of the NLO calculations still constantly overestimate the cross section by up to 20%, while – in the bounds of the available statistics – the shape of the measured jet spectrum is properly reproduced in the NLO calculations.

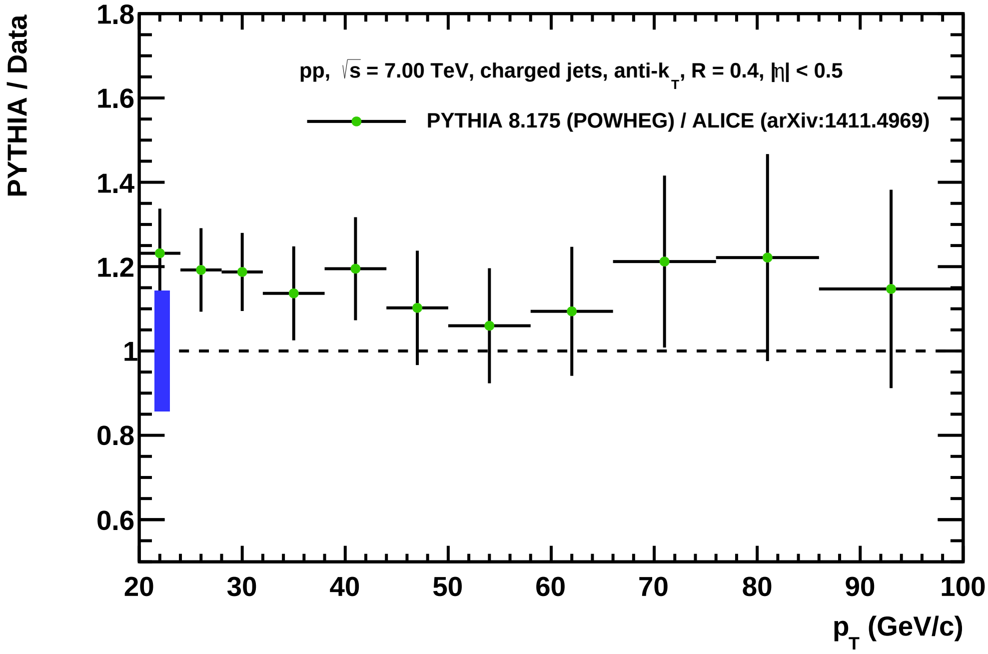

Figure 5.4: Ratio of charged jet spectra at 7.00 TeV from POWHEG+PYTHIA and ALICE. The ALICE spectrum is published in [A+14a]. Reconstructed with $R = 0.4$. Statistical and systematic uncertainties of the ALICE data have been summarised. The same comparison is shown in fig. 4.19 for PYTHIA stand-alone calculations. The blue bar marks the systematic uncertainty from settings in the POWHEG calculations.

6 Calculations for p+Pb Collisions

6.1 Effect of a Moving Centre-of-Mass System on Jet Spectra

In the beginning of 2013 the LHC collided lead ions and protons at $\sqrt{s_{\mathrm{NN}}} = 5.02$ TeV. Due to the two-in-one dipole design of the magnets in the main ring, the forces acting on the two beams are symmetrical. Thus the Pb beam energy per nucleon is fixed to $Z/A = 82/208$ of the proton beam energy. The total collision energy fulfils under the use of the first Mandelstam variable

$$E_{\mathrm{NN}}^2 = s_{\mathrm{NN}} = (\mathbf{p}_{\mathrm{Pb}} + \mathbf{p}_{\mathrm{p}})^2, \tag{6.1}$$

where $\mathbf{p}$ are the four-momenta of the proton and of a nucleon from the lead ion, respectively. The metric tensor in the Minkowski spacetime is chosen as $g_{\mu\nu} = \mathrm{diag}(-1, 1, 1, 1)$; furthermore the product of four-vectors is defined as $\mathbf{p}^2 = g_{\mu\nu} p^\mu p^\nu$. In the ultra-relativistic case, the nucleon mass in $E = \sqrt{p^2 + m^2}$, wherein $p = |\overrightarrow{p}|$ is the norm of the 3-momentum, can be neglected and so in total one obtains

$$\sqrt{s_{\mathrm{NN}}} = \sqrt{4 E_{\mathrm{Pb}} E_{\mathrm{p}}}. \tag{6.2}$$

Under the use of the known energy ratio $E_{\mathrm{Pb}} = \frac{82}{208} E_{\mathrm{p}}$ in a binary nucleon collision, this equation yields $\sqrt{s_{\mathrm{NN}}} = \sqrt{\frac{41}{26}} E_{\mathrm{p}}$. The asymmetric momenta result in a centre-of-mass system which is moving with respect to the lab frame. Let now the direction of the lead ion be positive in z direction and the direction of the proton negative. Thus one gets for the velocity β of this centre of mass, still neglecting the masses of the projectiles:

$$\beta = \frac{p_{\mathrm{CM}}}{E_{\mathrm{CM}}} = \frac{E_{\mathrm{Pb}} - E_{\mathrm{p}}}{E_{\mathrm{Pb}} + E_{\mathrm{p}}}, \tag{6.3}$$

from which follows, using the known energy ratio of the colliding nucleons, $\beta = \frac{82/208-1}{82/208+1} = -0.434$, meaning a movement of the centre of mass in the direction of the proton beam. The velocity can be expressed by means of the rapidity

$$y_{\mathrm{NN}} = 0.5 \cdot \ln \frac{1+\beta}{1-\beta} \tag{6.4}$$

as $y_{\mathrm{NN}} = -0.465$. In the ultra-relativistic limit, this is equivalent to a pseudorapidity shift applied to all generated particles, $\eta_{\mathrm{Lab}} = \eta_{\mathrm{CMS}} + y_{\mathrm{NN}}$. See also [KSS+10] for the used kinematic variables.

For comparing the p_{T} spectra from p+Pb collisions with those from a p+p reference, it is of interest to examine the effects of the moving collision CMS. Following, jet spectra from symmetrical and from Lorentz-boosted ($y_{\mathrm{Lab}} = 0.465$) collisions are shown. The calculations are done both with PYTHIA and with POWHEG+PYTHIA.

A rapidity shift can be applied to PYTHIA calculations by simply setting the proper beam energies in the initial configuration, which are in the aforementioned p+Pb scenario 1.577 plus 4.000 TeV for a total energy of 5.02 TeV and 2.198 plus 5.574 TeV for 7.00 TeV, respectively. In contrast, the POWHEG BOX framework allows to set symmetrical beam energies only. Here it is possible to apply the Lorentz boost on the parton list, which is handled from the POWHEG to the appropriate interface of PYTHIA for showering and hadronisation. This list of scattered partons uses the LHE ("Les Houches Events" [ABB+06]) file format, which contains, i.a. energy and the momentum vector components in an accessible way. For this analysis the Lorentz boost

$$\begin{aligned} p'_x &= p_x, \\ p'_y &= p_y, \\ p'_z &= \gamma p_z - \gamma\beta E, \\ E' &= \gamma E - \gamma\beta p_z \end{aligned} \tag{6.5}$$

with the usual $\gamma = (\sqrt{1-\beta^2})^{-\frac{1}{2}}$ has been automated to a C++-based script, working directly on the LHE files. For the boost, $y_{\text{Lab}} = +0.465$ was set: the sign of the shift (and thus: the direction of the movement) has no influence on the spectrum, as long as the colliding particles are identical and no asymmetric detector conditions have to be taken into account. As a first control of this process, fig. 6.1 shows the distribution of charged particles from the PYTHIA output with respect to its pseudorapidity η. While the non-boosted collision is fully symmetrical in η, the boost of the centre of mass is clearly transferred to the angle of the outcoming particle distribution.

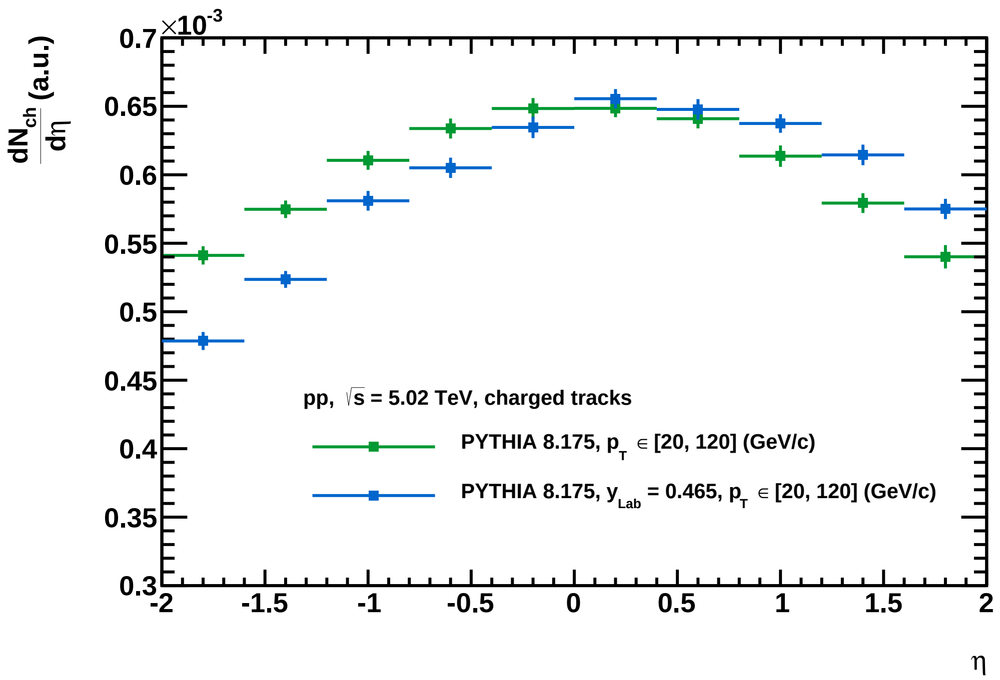

Figure 6.1: Pseudorapidity distributions of charged particles from PYTHIA at 5.02 TeV for symmetrical (2.510 + 2.510 TeV, black) and boosted (4.000 + 1.577 TeV, red) pp collisions. The Lorentz boost of the latter case implies a rapidity shift of $y_{\text{Lab}} = 0.465$.

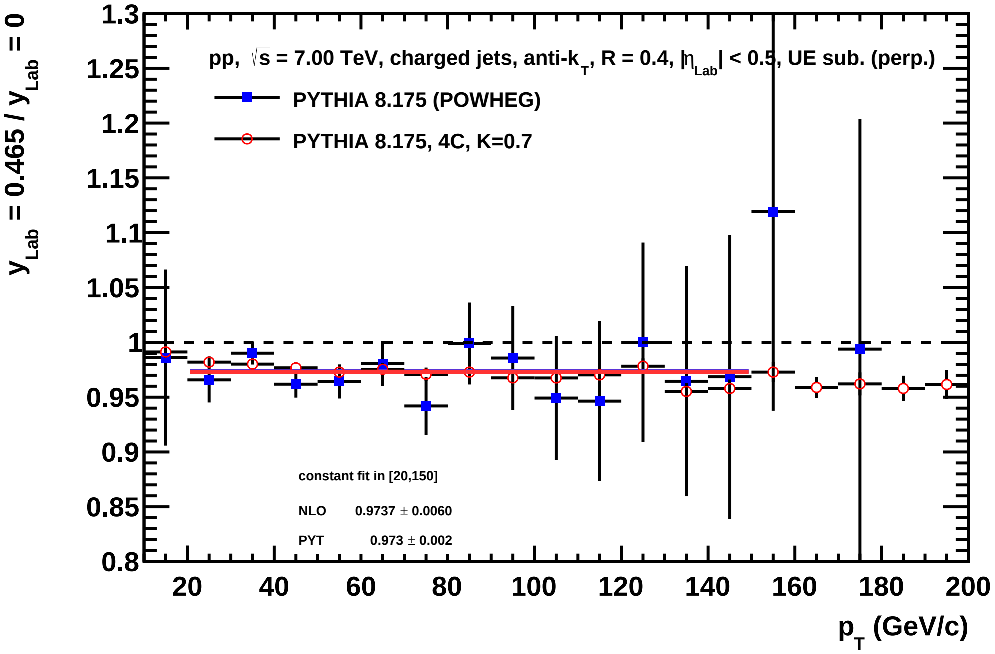

Figure 6.2: Ratio of charged jet spectra from 7.00 TeV from boosted ($y_{\mathrm{Lab}} = 0.465$) over symmetrical pp collisions. The collisions have been calculated in pure PYTHIA (red) and POWHEG+PYTHIA (blue), respectively. Constant fits in the p_{T} range from 20 to 150 GeV are shown with (coinciding) lines.

In the following, the rapidity shift is investigated concerning its effect on jet spectra, which are clustered from charged particle collections. Due to the different implementation in pure PYTHIA (tune 4C with a K-factor of 0.7, see sec. 4.4.2) and POWHEG+PYTHIA, both generation types are compared in fig. 6.2. General deviations between LO and NLO cancel out, since numerator and denominator originate each from the same generation type. Furthermore all jet collections are corrected for the underlying-event with the perpendicular cone method as described in sec. 4.2.3 in order to avoid any influence from background effects. A constant fit to the ratio "boosted over symmetrical" charged jet spectra for p_{T} from 20 to 150 GeV delivers 0.973 ± 0.002 for the PYTHIA (LO) data set and 0.974 ± 0.006 for the POWHEG+PYTHIA (NLO) calculation. The fit uncertainties are plainly small compared to the full uncertainties, as visible in the statistical fluctuations and thus uncertainties from the choice of the fitting range, as well as from further systematics in the overall calculation. On the other hand as a result, the effect of the moving centre-of-mass system clearly matches between both boosting mechanisms in LO and NLO.

In addition, the boosted/symmetrical ratio for collisions at 5.02 and 7.00 TeV has been compared from pure PYTHIA (LO) calculations, as it is shown in fig. 6.3. The results from both energies agree within their statistical uncertainties for all except one data point, but the effect seems to be consistently stronger at the lower energy: the effect from the boost at 7.00 TeV on the charged jets is of the order of -3%, and is of the order of -4% at 5.02 TeV. Reasons for the energy dependence of this suppression by the boost can be found in an energy dependence of the rapidity distribution, which is shifted within its cut borders by the Lorentz boost. For mid-p_{T} regions between 40 and 140 GeV, the shape of the correction can be neglected within its statistical uncertainties.

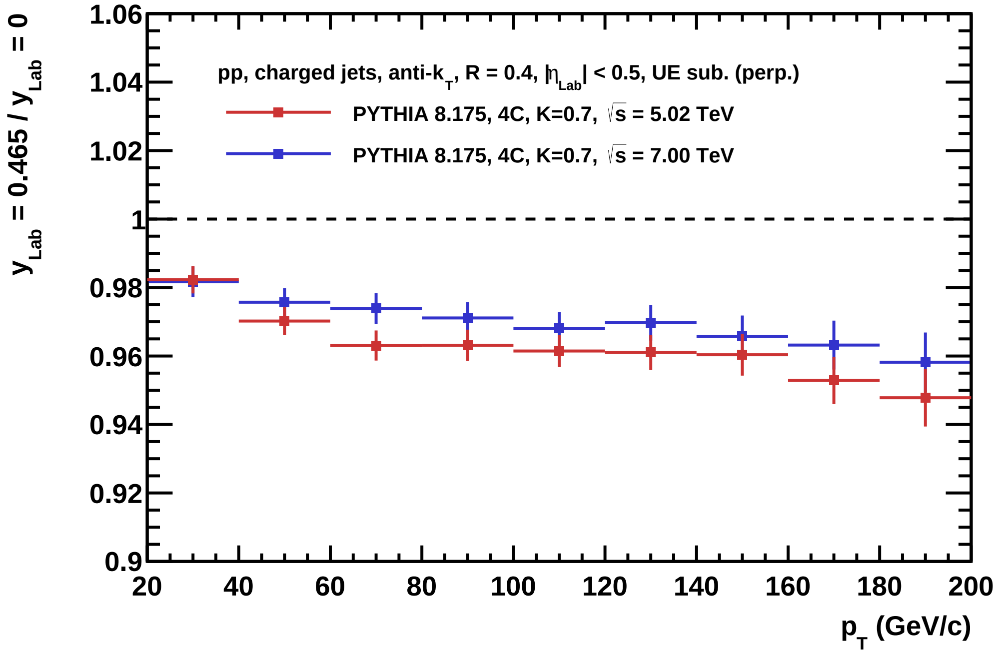

Figure 6.3: Ratio of charged jet spectra from boosted ($y = 0.465$) over symmetrical pp collisions at 5.02 and 7.00 TeV.

6.2 Jet Energy Scaling Function for a 5.02 TeV p+p Reference in LHC p+Pb Collisions

A scaling function from 7.00 TeV to 5.02 TeV p+p jet spectra has already been motivated in sec. 4.3: since no measurements from p+p collisions at 5.02 TeV are available, a data-based p+p reference for the p+Pb collisions at 5.02 TeV can only be constructed by scaling a measured spectrum from another centre-of-mass energy. In addition, the moving centre of mass of the p+Pb collisions has to be taken into account. The effect of this rapidity asymmetry of the particle production on jet spectra has been examined in the previous section and is shown in fig. 6.3.

A combined scaling function for the construction of a p+p reference in p+Pb jet analyses can be obtained by dividing a jet spectrum from PYTHIA p+p calculations at 5.02 TeV which include a direct Lorentz boost of $y = 0.465$ as described in the previous section, by a symmetrical 7.00 TeV p+p jet spectrum:

$$f(p_\mathrm{T}) = \frac{\mathrm{d}^2\sigma_\mathrm{jets}^{\text{PYTHIA: pp, 5.02 TeV, } y_\mathrm{Lab}=0.465}(p_\mathrm{T})/\mathrm{d}p_\mathrm{T}\mathrm{d}\eta}{\mathrm{d}^2\sigma_\mathrm{jets}^{\text{PYTHIA: pp, 7.00 TeV, } y_\mathrm{Lab}=0}(p_\mathrm{T})/\mathrm{d}p_\mathrm{T}\mathrm{d}\eta}. \tag{6.6}$$

The choice of a scaling from 7.00 TeV is equivalent with the claim for the smallest extrapolation step to 5.02 TeV among all available p+p energies, in order to minimize uncertainties from the energy scaling itself. $f(p_\mathrm{T})$ is shown for the anti-k_T jet finder radii $R = 0.2$ as well as $R = 0.4$ calculated from charged jets in fig. 6.4 and from full jets in fig. 6.5. The p+p collisions have been calculated with PYTHIA 8.175, which was set to tune t205 (tune 4C with $K = 0.7$) according to the results in sec. 4.4.2. The spectra at the different energies are generated independently; the overall statistical uncertainties are shown in the plots. Systematic uncertainties without a significant energy or boosting dependence cancel out. The systematic uncertainties of PYTHIA's energy scaling cannot be consequently deduced. The deviation of up to about 40% between PYTHIA's best tunings in comparison with data at 2.76 TeV and at 7.00 TeV can only be understood as an upper limit due to the significantly smaller span between 5.02 TeV and 7.00 TeV in this calculation. The real scaling function may be slightly larger than the PYTHIA based result. Also the particle composition from PYTHIA and the energy scaling of different particle species have not been investigated here. Especially pion contributions will be examined in an upcoming thesis [Sch15]. Uncertainties from the effect of the moving centre of mass of the collided system cannot directly be checked to data, since no collisions in this energy domain have been performed symmetrically <u>and</u> asymmetrically. A precisely calculated boost of measured data requires full particle identification to convert between rapidity and pseudorapidity.

For the charged jet case, the single jet spectra, hence numerator and denominator of f, are shown in fig. 6.6 and 6.7. When applying the scaling functions to measured 7.00 TeV data, it should be paid attention to ensure comparable conditions in the p+p and p+Pb jet reconstructions.

For the ALICE publication [A$^+$15] of the nuclear modification factor from jets (compare eq. 2.5) in p+Pb collisions at $4000 + 1577$ GeV, charged jets from 7.00 TeV have been scaled to 5.02 TeV based on POWHEG+ PYTHIA calculations. The boost of $y_\mathrm{Lab} = 0.465$ has been applied to the POWHEG data at 5.02 TeV in the same way as in sec. 6.1 prior to fragmentation and showering in PYTHIA. The used NLO scaling function is shown in fig. 8.3 of [Haa15b] (compare the LO "charged" scaling function of this work, fig. 6.4). The overall resulting scaled 5.02 TeV p+p jet spectrum has been used as a reference for the p+Pb charged jet spectrum. [A$^+$15] and [Haa15b] present an R_pPb for p_T between 20 and 100 TeV, which is compatible with unity for both jet finder resolutions $R = 0.2$ and $R = 0.4$. This is interpreted as compatibility with the absence of strong modifications of the initial parton distribution or strong final-state effects.

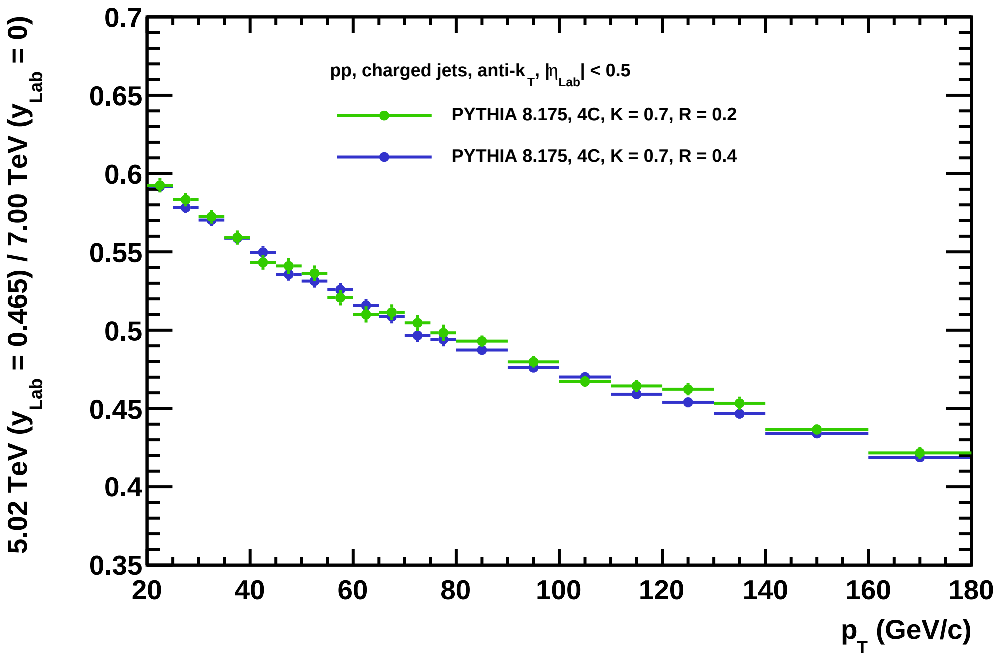

Figure 6.4: Energy scaling function for charged jet spectra from symmetrical pp collisions at 7.00 TeV to pp at 5.02 TeV with a moving centre-of-mass system ($y_{\mathrm{Lab}} = 0.465$). The function enables the calculation of a pp reference jet spectrum for 5.02 TeV pPb collisions at LHC conditions from a known 7.00 TeV pp jet spectrum. Determined from the PYTHIA jet spectra in fig. 6.6 and 6.7.

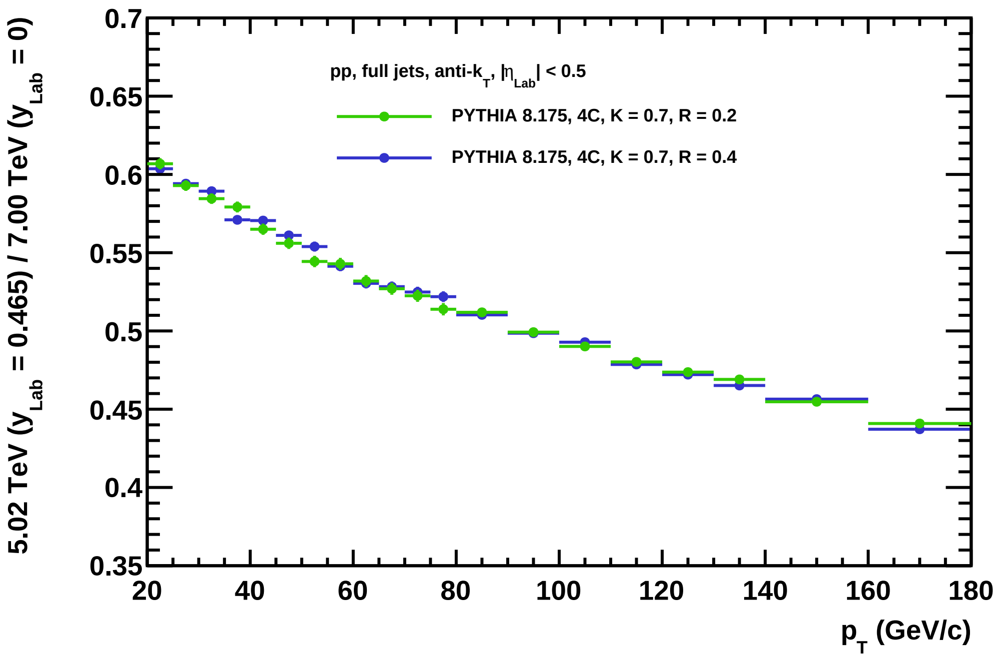

Figure 6.5: Energy scaling function for full jet spectra from symmetrical pp collisions at 7.00 TeV to pp at 5.02 TeV with a moving centre-of-mass system ($y_{\mathrm{Lab}} = 0.465$). The function enables the calculation of a pp reference jet spectrum for 5.02 TeV pPb collisions at LHC conditions from a known 7.00 TeV pp jet spectrum.

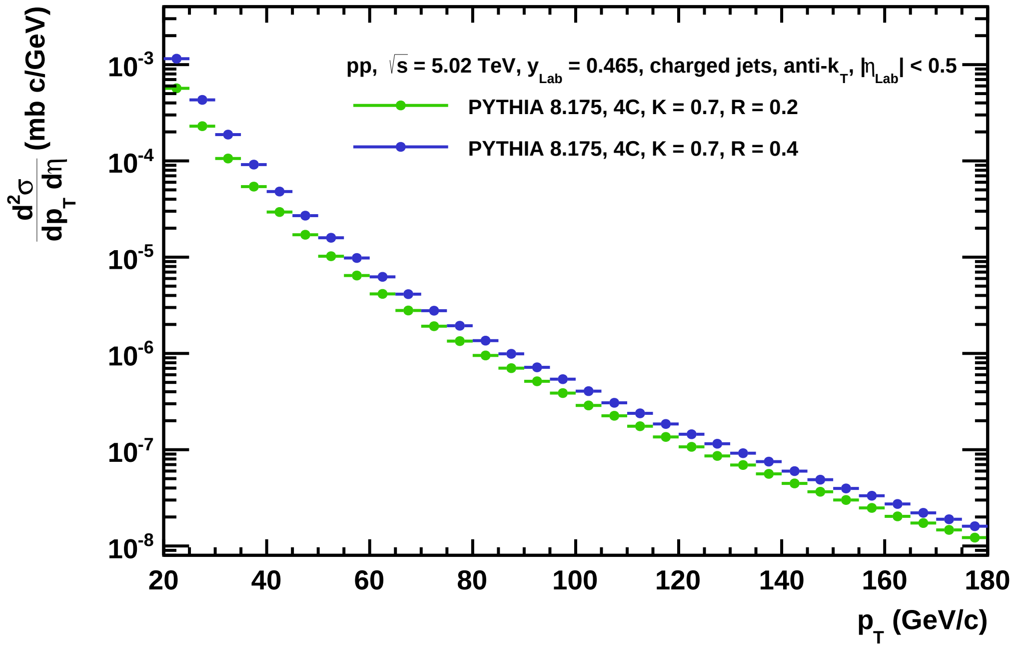

Figure 6.6: Charged jet spectra from pp collisions at 5.02 TeV generated with PYTHIA 8.175, tune 4C with a K-factor of 0.7. The centre-of-mass system of the collision system has been set to a rapidity of $y_{\mathrm{Lab}} = 0.465$. Anti-k_{T} jet reconstruction with $R = 0.2$ and $R = 0.4$, corrected for the underlying-event with the perpendicular cone method as described in sec. 4.2.3.

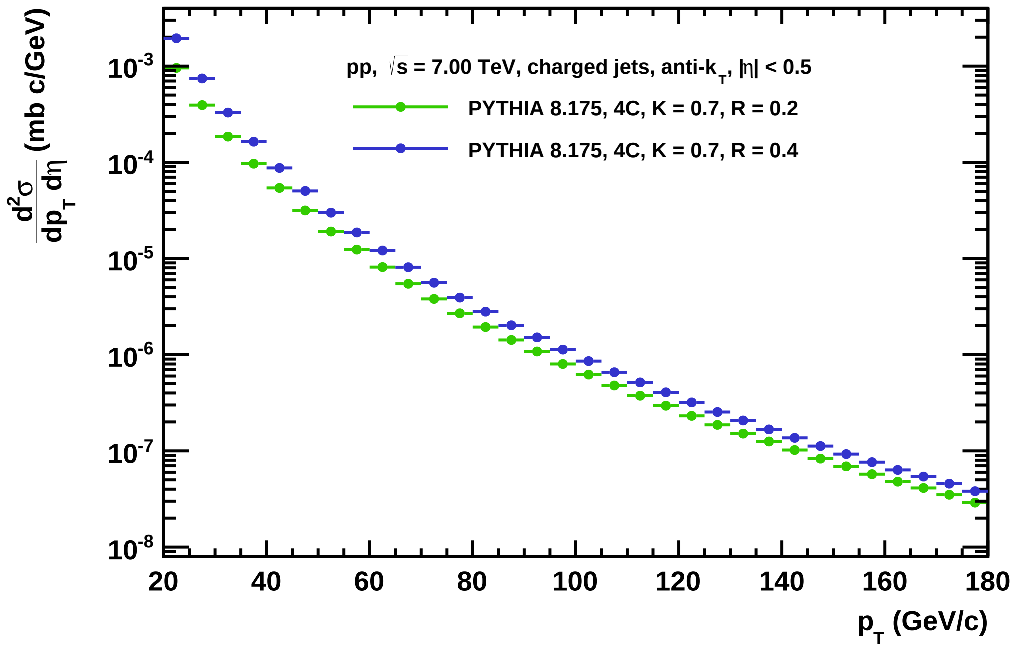

Figure 6.7: Charged jet spectra from symmetrical pp collisions at 7.00 TeV generated with PYTHIA 8.175, tune 4C with a K-factor of 0.7. Anti-k_{T} jet reconstruction with $R = 0.2$ and $R = 0.4$, corrected for the underlying-event with the perpendicular cone method as described in sec. 4.2.3.

7 Summary

In the first part of this thesis, several possible contributions to systematic uncertainties of jet spectra have been investigated. Some of the probed influences appear in spectra from PYTHIA Monte Carlo calculations, while others are relevant in jet analyses of measured data from collider experiments in the same way. Since different settings and conditions can potentially significantly change the resulting jet spectrum, the knowledge of their effects is important both to ensure comparability of different spectra and to reliably interpret single jet spectra. The investigated uncertainties have been discussed in the local working group during preparations for the publication of a nuclear jet modification factor $R_{\mathrm{pPb}}(p_{\mathrm{T}})$ at 5.02 TeV [A+15].

All tests in this part have been performed under the use of spectra from proton–proton collisions, which have been calculated with the PYTHIA Monte Carlo event generator in version 8.175; jets have been clustered via the (anti-)k_{T} algorithm of the FastJet package in version 2.4. The settings to be probed were available through the flexibility of this event generation and analysis framework in a statistical precision that could not have been easily reached from data records at real collider experiments.

A "software trigger", which is often used in PYTHIA calculations to reduce the necessary storage size is defined as the requirement for each accepted event, to contain at least one full jet with $p_{\mathrm{T}} > 10$ GeV within $|\eta| < 1.5$ from anti-k_{T} reconstruction with $R = 1.0$. It could be shown that this trigger does not affect charged or full jet spectra above a transverse jet momentum of 10 GeV, reconstructed both via the anti-k_{T} algorithm with $R = 0.2$ and $R = 0.4$ from calculated p+p collisions at 2.76, 5.02 or 7.00 TeV.

Concerning recombination schemes for momenta in the FastJet anti-k_{T} algorithm, the differences between the boost-invariant p_{T} scheme and the p_{T} scheme turned out to be negligible above a transverse jet momentum of roughly 15 GeV. Below this value, the differences between energy and momentum of measured/calculated particles lead to deviations, especially from pions ($m_{\pi^{\pm}} = 139.6$ MeV [O+14]) in the jets. Furthermore it could be shown that the CPU time for the jet clustering in the used framework can be reduced by at least 10% by using the boost-invariant p_{T} scheme and manually setting $E = p$ for all particles: the resulting jet spectra are identical to spectra reconstructed with the p_{T} scheme.

Combinatorial jets can in general be reduced by requiring a minimum jet area, which is realised by applying an area cut to the final jet collection. The typical cut threshold is $0.6\pi R^2$, where R is the jet finder resolution parameter. Neither full nor charged anti-k_{T} jet spectra with $R = 0.2$ or $R = 0.4$ from PYTHIA p+p calculations at 5.02 and 7.00 TeV showed a relevant modification from the area cut in the analysed p_{T} range between 20 and 120 GeV. The most probable value in jet area distributions appeared very near to πR^2, while less than 0.1% of the jets are affected from a cut at $0.6\pi R^2$.

Two different underlying-event corrections of jet spectra from PYTHIA p+p collisions have been compared to uncorrected jet spectra from the same PYTHIA p+p calculations. The approach $p_{\mathrm{T}}^{corrected} = p_{\mathrm{T}} - \rho A_{\mathrm{Jet}}$ with a constant, homogeneous background density ρ reduces the momentum of each jet depending only on its area A_{Jet}. In contrast, the "perpendicular cones" method estimates a background density individually for each collision event. Both corrections cause a clear reduction of the corrected jet spectrum especially at $p_{\mathrm{T}} < 50$ GeV. The decrease is more pronounced from the constant subtraction. Both methods are not fully compatible and should therefore be matched between jet reconstructions, before spectra are compared.

Another major source of uncertainties in spectra calculated with the PYTHIA Monte Carlo event generator originates from the program itself, since many internal parameters need to be tuned in comparison to measured data. The general tunes of PYTHIA 8.175 and two own settings have been investigated. Jet spectra from the differently tuned PYTHIA calculations deviate by up to ±30% compared to tune 4C. It could be shown that the best agreement between jet spectra from ALICE p+p measurements and such from PYTHIA p+p calculations is reached with PYTHIA's tune 4C (at 2.76 TeV) and with tune 4C plus an additional K-factor scaling of the hard cross-section of 0.7 (at 7.00 TeV). Enhancements in extensive future tunings are possible to be achieved by finding a verified setting of α_s in the different sections of PYTHIA, and especially by a matching based on more detailed observables as e.g. the particle composition.

The PYTHIA+FastJet framework can be used to generate jet scaling functions. These functions can be matched in a highly flexible way for the scaling between jet spectra at different energies and with deviating other conditions. In this work, scaling functions for the calculation of a 5.02 TeV p+p jet spectrum to be applied as a reference for asymmetrical ($y = 0.465$) p+Pb jet spectra are presented for p_T between 20 and 180 GeV both for full as well as for charged jets with anti-k_T jet finder parameters $R = 0.2$ and $R = 0.4$. After the reference calculation based on a measured 7.00 TeV jet spectrum, the resulting 5.02 TeV spectrum can directly be used as p+p baseline to obtain a nuclear modification factor in p+Pb collisions. Adaptions of the scaling function to different physics and analysis cases can easily be reached within the available framework.

For the calculation of absolute values in jet spectra, the superiority of NLO calculations could be shown. In general, effort should be invested to establish a stable framework, which ensures the physically solid matching of NLO event generators to subsequent, model-based Shower Monte Carlo programs like PYTHIA.

Furthermore, the effect of the moving centre-of-mass system in p+Pb collisions on jet spectra has been investigated in detail as a function of p_T. For the p+Pb collisions at 5.02 TeV as recorded with ALICE, the effect could be shown to be of the order of a 4% decrease compared to jet spectra from symmetrical collisions. As a consequence of these investigations, a program could be provided to universally apply Lorentz boosts to LHE files, as used to transfer POWHEG NLO calculations to SMC programs for showering and fragmentation like PYTHIA.

Bibliography

[A+08] *ALICE* collaboration, K. Aamodt et al. *The ALICE experiment at the CERN LHC*. *Jinst*, 3, S08002, doi:10.1088/1748-0221/3/08/S08002, 2008.

[A+11a] *ALICE* collaboration, K. Aamodt et al. *Charged-particle multiplicity density at mid-rapidity in central Pb–Pb collisions at* $\sqrt{s_{NN}} = 2.76$ *TeV*. arXiv:1011.3916, 2011.

[A+11b] *ALICE* collaboration, B. Abelev et al. *Underlying Event measurements in pp collisions at* $\sqrt{s} = 0.9$ *and 7 TeV with the ALICE experiment at the LHC*. arXiv:1112.2082, 2011.

[A+12a] *ALICE* collaboration, B. Abelev et al. *Measurement of Event Background Fluctuations for Charged Particle Jet Reconstruction in Pb–Pb collisions at* $\sqrt{s_{NN}} = 2.76$ *TeV*. arXiv:1201.2423, 2012.

[A+12b] *ALICE* collaboration, B. Abelev et al. *Transverse Momentum Distribution and Nuclear Modification Factor of Charged Particles in p–Pb Collisions at* $\sqrt{s} = 5.02$ *TeV*. arXiv:1210.4520, 2012.

[A+13a] *ALICE* collaboration, B. Abelev et al. *Energy Dependence of the Transverse Momentum Distributions of Charged Particles in pp Collisions Measured by ALICE*. arXiv:1307.1093, 2013.

[A+13b] *ALICE* collaboration, B. Abelev et al. *Measurement of the inclusive differential jet cross section in pp collisions at* $\sqrt{s} = 2.76$ *TeV*. arXiv:1301.3475, 2013.

[A+14a] *ALICE* collaboration, B. Abelev et al. *Charged jet cross sections and properties in proton-proton collisions at* $\sqrt{s} = 7$ *TeV*. arXiv:1411.4969, 2014.

[A+14b] *ALICE* collaboration, B. Abelev et al. *Performance of the ALICE Experiment at the CERN LHC*. arXiv:1402.4476, 2014.

[A+15] *ALICE* collaboration, J. Adam et al. *Measurement of charged jet production cross sections and nuclear modification in p–Pb collisions at* $\sqrt{s_{NN}} = 5.02$ *TeV*. arXiv:1503.0681, 2015.

[ABB+06] J. Alwall, A. Ballestrero, P. Bartalini, S. Belov, E. Boos, A. Buckley, J. Butterworth, L. Dudko, S. Frixione et al. *A standard format for Les Houches Event Files*. arXiv:hep-ph/0609017, 2006.

[AGI+83] B. Andersson, G. Gustafson, G. Ingelman and T. Sjöstrand. *Parton Fragmentation and String Dynamics*. *Physics Reports*, 97:31–145, doi:10.1016/0370-1573(83)90080-7, 1983.

[ANO+10] S. Alioli, P. Nason, C. Oleari and E. Re. *A general framework for implementing NLO calculations in shower Monte Carlo programs: the POWHEG BOX*. arXiv:1002.2581, 2010.

[ANO+11] S. Alioli, P. Nason, C. Oleari and E. Re. *The POWHEG BOX user manual: common features*. 2011.

[BO90] J.-P. Blaizot and J.-Y. Ollitrault. *Hydrodynamics of Quark-Gluon Plasmas*. *Commis. énerg., Institut de physique théorique*, Saclay, 1990.

[Buc14] A. Buckley. *Les Houches 2013: Physics at TeV Colliders: SM Working Group*. arXiv:1405.1067, 2014.

[CPE00] CPEP. *Standard Model of Fund. Particles & Interactions*. Contemporary Physics Education Project, Berkeley National Laboratory, `http://www.pha.jhu.edu/~dfehling/particle.gif`, 2000.

[CRS+10] M. Cacciari, J. Rojo, G. P. Salam and G. Soyez. *Jet Reconstruction in Heavy Ion Collisions*. CERN-PH-TH/2010-223, arXiv:1010.1759, 2010.

[Cse05] L. P. Csernai. *Introduction to Relativistic Heavy Ion Collisions*. `http://csernai.no`, 2005.

[CSS11] M. Cacciari, G. P. Salam and G. Soyez. *FastJet user manual (for version 3.0.6)*. CERN-PH-TH/2011-297, 2011.

[d'E09] D. d'Enterria. *Jet quenching*. *Landolt-Börnstein*, 1-23A:471, arXiv:0902.2011, 2009.

[EB08] L. Evans and P. Bryant. *(eds.), LHC Machine*. *Jinst*, 3, S08001, doi:10.1088/1748-0221/3/08/S08001, 2008.

[FNO07] S. Frixione, P. Nason and C. Oleari. *Matching NLO QCD computations with Parton Shower simulations: the POWHEG method*. arXiv:0709.2092, 2007.

[Fod02] Z. Fodor. *Lattice QCD Results at Finite Temperature and Density*. arXiv:hep-lat/0209101, 2002.

[For87] S. Fortune. *A Sweepline Algorithm for Voronoi Diagrams*. *Algorithmica*, 2, 1–4:153–174, 1987.

[Gar13] G. M. García. *Advances in Quark Gluon Plasma*. arXiv:1304.1452, 2013.

[Haa15a] R. Haake. *Email exchange*. February 2015.

[Haa15b] R. Haake. *Measurement of charged jets in p–Pb collisions at* $\sqrt{s_{NN}} = 5.02$ *TeV with the ALICE detector*. Doctoral Thesis, WWU, Münster, 2015.

[KB13] C. Klein-Bösing. *Study of the Quark-Gluon Plasma with Hard and Electromagnetic Probes*. Habilitation Treatise, WWU, Münster, 2013.

[KSS+10] M. Kliemant, R. Sahoo, T. Schuster and R. Stock. *Global Properties of Nucleus–Nucleus Collisions*, volume 785, 23–103 of *Lecture Notes in Physics*. Springer-Verlag, Berlin Heidelberg, 2010.

[Lef08] C. Lefèvre. *CERN's accelerator complex*. `http://cds.cern.ch/record/1260465`, CERN-DI-0812015, 2008.

[Mü13] G. Münster. *Quantenchromodynamik*. Lecture. WWU, Münster, 2013.

[Nas04] P. Nason. *A New Method for Combining NLO QCD with Shower MC Algorithms*. arXiv:hep-ph/0409146, 2004.

[NLC+08] P. M. Nadolsky, H.-L. Lai, Q. H. Cao, J. Huston, J. Pumplin, D. Stump, W.-K. Tung and C.-P. Yuan. *Implications of CTEQ global analysis for collider observables*. arXiv:0802.0007, 2008.

[O+14] K. A. Olive et al. *Particle Data Group*. *Chin. Phys.*, C38, 090001, `http://pdg.lbl.gov`, 2014.

[Per00] D. H. Perkins. *Introduction to High Energy Physics*. Cambridge University Press, 2000.

[PSH+02] J. Pumplin, D. R. Stump, J. Huston et al. *New Generation of Parton Distributions with Uncertainties from Global QCD Analysis*. arXiv:hep-ph/0201195, 2002.

[R+12] *ALICE* collaboration, K. Reygers et al. *A Quick Tour of Ultra-Relativistic Heavy-Ion Physics at the LHC*. arXiv:1208.1626, 2012.

[RT13] J. Rak and M. J. Tannenbaum. *High* p_T *Physics in the Heavy Ion Era*. Cambridge University Press, 2013.

[SAC+14] T. Sjöstrand, S. Ask, J. R. Christiansen, R. Corke, N. Desai, P. Ilten, S. Mrenna, S. Prestel, C. O. Rasmussen and P. Z. Skands. *An Introduction to PYTHIA 8.2*. arXiv:1410.3012, 2014.

[Sat10] H. Satz. *The Thermodynamics of Quarks and Gluons*, volume 785, 1–21 of *Lecture Notes in Physics*. Springer-Verlag, Berlin Heidelberg, 2010.

[SC10] T. Sjöstrand and R. Corke. *Interleaved Parton Showers and Tuning Prospects*. arXiv:1011.1759, 2010.

[SCD+15] T. Sjöstrand, J. R. Christiansen, N. Desai, P. Ilten, S. Mrenna, C. O. Rasmussen, S. Prestel, P. Skands, S. Ask and R. Corke. *PYTHIA - The Lund Monte Carlo (Online Manual, version 8.2)*. `http://home.thep.lu.se/~torbjorn/pythia82html/Welcome.html`, 2015.

[Sch15] L. Schlüter. Bachelor Thesis, to be published, WWU, Münster, 2015.

[SMS07] T. Sjöstrand, S. Mrenna and P. Skands. *A Brief Introduction to PYTHIA 8.1*. arXiv:0710.3820, 2007.

[Vaj13] M. Vajzer. *Email exchange*. June 2013.

[Won94] C.-Y. Wong. *Introduction to High-Energy Heavy-Ion Collisions*. World Scientific Publishing, Singapore, 1994.

Danksagung / Acknowledgements

Ich danke Prof. Dr. Johannes Wessels für alle eingerichteten Möglichkeiten, die hervorragende Atmosphäre in seiner, unserer Arbeitsgruppe und die Unterstützung dieser Arbeit. Besonders danke ich PD Dr. Christian Klein-Bösing für die umfassende Anleitung, Beratung und Diskussionen, außergewöhnliche Geduld und die stets offene Tür. Der ganzen Arbeitsgruppe danke ich für vielfältige Hilfen und die gute Stimmung, besonders hier Dr. Bastian Bathen und Dr. Markus Heide für kritische Durchsicht und Besprechung von Inhalten sowie Dr. Rüdiger Haake für die Beantwortung von Fragen. Danke ebenso an Hendrik Poppenborg für hilfreiche Diskussionen. Thanks to Dr. Denise Moreira de Godoy for helpful answers. Danke an Dr. Oliver Busch für das Zusenden von Daten. Many thanks to Michal Vajzer for calculations from a POWHEG and explanations. Ferner danke ich sehr meinen Eltern, die dieses Studium so und so überhaupt erst ermöglicht und es stets unterstützt haben. My particular thanks to Tony Rublon for the deeply helpful exchange.

Printed on 100% recycled paper.